UNIVERSITY OF TWENTE.

MESA+
INSTITUTE FOR NANOTECHNOLOGY

Master's thesis

Highly anisotropic transport properties at interfaces of oxides

Peter Brinks
Enschede, May 20th 2010
Applied Physics
University of Twente
Faculty of Science and Technology
Inorganic Materials Science

Graduation committee:

Prof. dr. ing. Dave H.A. Blank
Prof. dr. ing. Hans Hilgenkamp
Dr. ir. Alexander Brinkman
Dr. ir. Gertjan Koster
Dr. ir. Mark Huijben

Abstract

Due to the unique properties of interfaces of complex oxides, these interfaces are extensively studied. As an example, the interface between the two wide band gap insulators $SrTiO_3$ and $LaAlO_3$ can become conducting, depending on the interface configuration.

So far, only conducting $SrTiO_3$ /$LaAlO_3$ interfaces have been grown on single crystal $SrTiO_3$ substrates. The aim of this research is to grow conducting $SrTiO_3$/LAO interfaces on a different substrate material and to study their electronic properties. This approach provides the possibility to investigate the role of the quality and thickness of the underlying $SrTiO_3$ layer.

$LaSrAlTaO_3$ substrates were used for this research, and an annealing procedure was developed which results in a well defined step and terrace structure with unit cell step heights. On these substrates, conducting $SrTiO_3$/LAO heterostructures were successfully deposited.

The electronic properties of the deposited heterostructures showed highly anisotropic behavior. Differences in resistance up to one order of magnitude were observed. The origin of this strong directional anisotropy was found in the direction of the step and terrace structure at the interface. This observation in combination with the strength of the anisotropy led to the conclusion that the conduction is limited to a two-dimensional region at the interface. For these samples a sheet carrier density of typically $2 \cdot 10^{14}\ cm^{-2}$ is measured, which corresponds to 0.3 electrons per unit cell. Carrier mobilities of the order of 1 $cm^2V^{-1}s^{-1}$ are measured.

For deposition of the $LaAlO_3$ layer at low oxygen pressures ($10^{-6}\ mbar$) on $SrTiO_3$ substrates, a conducting $SrTiO_3$ layer is formed due to the formation of oxygen vacancies. This leads to a strong increase of the sheet carrier density. This behavior is not observed for heterostructures grown on $LaSrAlTaO_3$ substrates. A sheet carrier density of approximately $2 \cdot 10^{14}\ cm^{-2}$ at room temperature is measured for samples deposited at pressures between $10^{-4}\ mbar$ and $10^{-6}\ mbar$. For the samples grown at $10^{-5}\ mbar$ and $10^{-6}\ mbar$ the sheet carrier density remains constant between 2 K and 300 K, which is not observed for heterostructures grown on $SrTiO_3$ substrates. For samples grown at $10^{-4}\ mbar$ the sheet carrier density shows a strong decrease for temperatures below 50 K, indicating carrier freeze out. This behavior is comparable for samples grown on $SrTiO_3$ substrates.

The anisotropy, sheet carrier density and mobility are measured for various thicknesses of the $SrTiO_3$ layer. For all these samples a strong anisotropy is observed, and an overall increase in resistance is observed for thinner $SrTiO_3$ layers. For a thickness of 10 ML and 20 ML of $SrTiO_3$, a constant sheet carrier density between 2 K and 300 K is observed. For a thickness of 5 ML of $SrTiO_3$ the sheet carrier density decreases below 50 K, indicating carrier freeze out. The differences in resistance are caused by differences in mobility. To study the influence of the quality of the $SrTiO_3$ layer, samples with a hybrid molecular beam epitaxy (hybrid MBE) STO layer were also included. For these samples a lower resistance was observed, caused by an increase of the carrier mobility. Based on these results it is concluded that the quality of the $SrTiO_3$ layer plays an important role for the electronic properties and especially for the carrier mobility.

Contents

Chapter 1

Introduction

Materials within the class of complex oxides exhibit several interesting properties, such as ferroelectricity and ferromagnetism. The presence of these properties led to intensified research on complex oxide materials after the Second World War. However, after the discovery of high-temperature superconductivity of $YBa_2Cu_3O_{7-x}$ in 1986, the interest in all types of complex oxides increased even more and much research has been done on these materials.[1, 2, 3]

A new branch of research opened after the first publication of a two-dimensional high mobility electron gas at the $SrTiO_3$/$LaAlO_3$ interface, by Ohtomo and Wang.[4] Since this discovery, much research has been devoted to explain and tune the unique properties at several different interfaces of perovskite materials.[5, 6] Although no complete understanding of the interface effects is available, the properties can be tuned by, for example, varying the deposition pressure during growth. In addition to the deposition parameters, the interface properties strongly depend on the surface termination of the substrate. A short overview of the relevant properties of $SrTiO_3$/$LaAlO_3$ interfaces is given in chapter 2.

To further investigate the interface properties, the aim of the work described in this project is to grow conducting $SrTiO_3$/$LaAlO_3$ interfaces on substrates of a different material. This can exclude the possible role of the underlying $SrTiO_3$ substrate and provides a tool to investigate the influence of the $SrTiO_3$ layer. If the conductivity originates from the interface, and is two-dimensional, one expects to observe a large directional anisotropy. After all, the interface consists of a step and terrace structure, which largely determines the morphology at the interface. In addition to the growth of conducting $SrTiO_3$/$LaAlO_3$ interfaces, an attempt was made to determine the origin of the conduction mechanism. This was done by varying deposition parameters and thickness of the grown layers. The goals of this research are:

- Grow conducting $SrTiO_3$/$LaAlO_3$ interfaces on a different substrate material
- Determine if there is a directional anisotropy for the conductivity and find the origin
- Determine the role of the underlying $SrTiO_3$ material by analyzing the electronic properties and comparing these results with samples grown on $SrTiO_3$ substrates

Because of the suitable crystal structure, $LaSrAlTaO_3$ was chosen as substrate material. No standard substrate treatment was available for $LaSrAlTaO_3$ to obtain a well-defined step and terrace structure at the surface. This made it necessary to start with an experimental study to determine a suitable substrate treatment. Information about $LaSrAlTaO_3$ and the results of the substrate treatment are described in chapter 3.

The process of growth and characterization of $SrTiO_3/LaAlO_3$ interfaces on $LaSrAlTaO_3$substrates is described in chapter 4. A description of the experimental techniques and some general properties of the samples are given. Additionally, a comparison is made with samples grown on $SrTiO_3$ substrates. The results of electronic characterizations of the samples are described in chapter 5 in more detail. Finally, the results are discussed in chapter 6.

Chapter 2

Perovskite materials and unique properties

The materials used for this research, $SrTiO_3$, $LaAlO_3$ and the substrate material $LaSrAlTaO_3$, have a perovksite structure. Perovskite is the name for the mineral $CaTiO_3$, which was first discovered in 1839 by Gustav Rose, in the Ural mountains in Russia and is named for the Russian mineralogist, Count Lev Aleksevich von Perovski. In addition to the mineral, the name perovskite also refers to a structural family. Materials with the same crystal structure as $CaTiO_3$, belong to the structural family of perovskites.[7] In this chapter, first an introduction about the structural properties of perovskites is given. Secondly, the unique properties at $SrTiO_3/LaAlO_3$ interfaces on $SrTiO_3$ substrates are described.

2.1 Structural properties of perovskites

Many oxides with the composition ABO_3, with A and B two different sized cations, belong to the perovskite structural family. The arrangement of ions is as shown in figure 2.1.[8] In this figure, the crystal structure of $SrTiO_3$ and $LaAlO_3$ is depicted.

At room temperature $SrTiO_3$ has a simple cubic structure with a lattice parameter of 3.905 Å. The titanium atoms are located at the corners of the cube, and the strontium atoms are positioned at the center of the cube. The oxygen atoms are located at the centers of the twelve cube edges. This structure leads to corner-shared strings of TiO_6 octahedra. These octahedra have 90° angles, and six equal Ti-O bonds at 1.952 Å. All strontium atoms are surrounded by twelve oxygen atoms, at equal distances of 2.761 Å. At a temperature of $\sim$110 K $SrTiO_3$ undergoes a second-order phase transition from cubic to tetragonal, which is caused by an opposite rotation of neighboring TiO_6 octahedra. The material can be described as $Sr^{2+}Ti^{4+}O^{2-}{}_3$ in the ionic limit.[7, 9]

$LaAlO_3$ consists of a rhombohedrally distorted perovskite structure at room temperature and undergoes a transition to the cubic perovskite structure at $\sim$813 K. The rhombohedral structure at room temperature can be described as pseudocubic, with a rotation of the AlO_6 octahedra. The lattice parameters of the unit cell are 3.791 Å and the aluminum and lanthanum atoms are placed at the corners and centers, respectively. In the ionic limit this material can be described as $La^{3+}Al^{3+}O^{2-}{}_3$.[9, 10, 11]

When studying surfaces and interfaces of perovskites, it is also useful to realize that the structure consists of a layered structure in the three principal directions. In general terms,

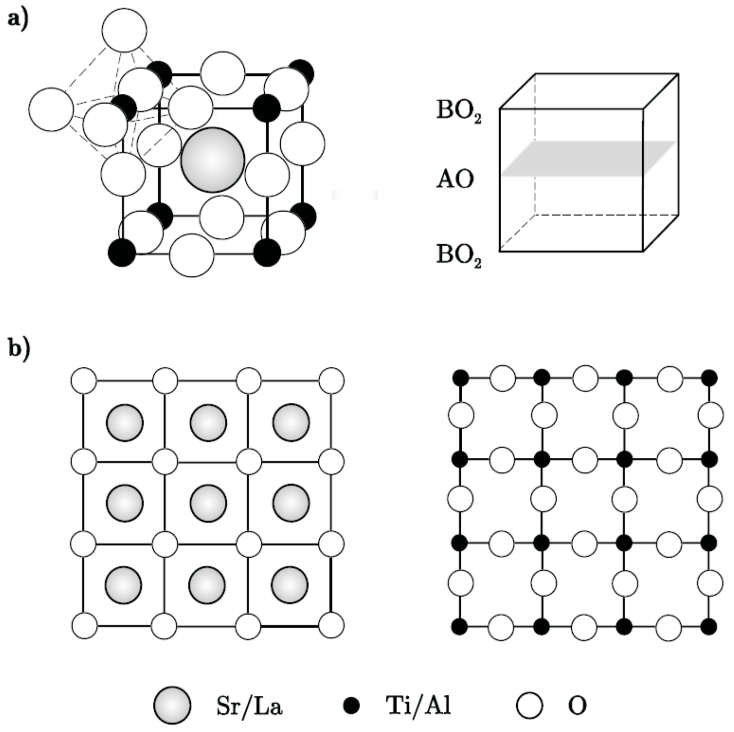

Figure 2.1 Perovskite crystal structure [8]

perovskites form a stack of alternating AO and BO$_2$ layers, as shown in figure 2.1. Because the stacking sequence is maintained in heterostructures, it is possible to construct two different types of interfaces by controlling the surface termination of the substrate. When the surface of the substrate is single terminated and consists of an AO layer, the first deposited layer will consist of BO$_2$ and vice versa. The physical properties, e.g. resistivity, of these two types of interfaces can be very different. For SrTiO$_3$ and LaAlO$_3$ these two different interfaces are shown in figure 2.2.

2.2 Unique properties at interfaces of complex oxides

Although the two different types of interfaces look structurally comparable, for SrTiO$_3$/LaAlO$_3$ interfaces there is an important difference. In SrTiO$_3$ the two different layers, Sr^{2+}O^{2-} and Ti^{4+}O$^{2-}{}_2$, are both charge-neutral. However, for LaAlO$_3$ the layers are alternatingly positively, La^{3+}O^{2-}, and negatively, Al^{3+}O$^{2-}{}_2$, charged.

In a SrTiO$_3$/LaAlO$_3$ heterostructure a polarity discontinuity forms at the interface, caused by the junction between a polar and a nonpolar plane. Figure 2.3 shows how such an interface leads to a polar catastrophe. If there is no reconstruction at the interface, the electrostatic potential diverges with thickness for both types of interfaces.[12]

In order to solve this polar catastrophe, a reconstruction appears at the interface. In traditional semiconductors, where all ions have a fixed valence, this reconstruction involves atomic disordering and stoichiometric change at the interface. Because the valence of ions in complex oxides is not fixed, another option is available. When it is energetically favorable, electrons are redistributed rather than atoms and the interface charge is compensated for by mixed valence.[12]

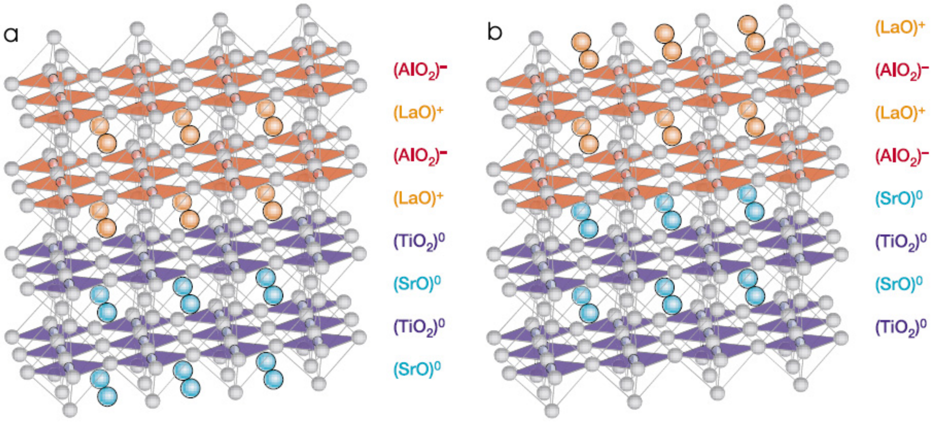

Figure 2.2 Two different $SrTiO_3/LaAlO_3$ interface configurations [4]

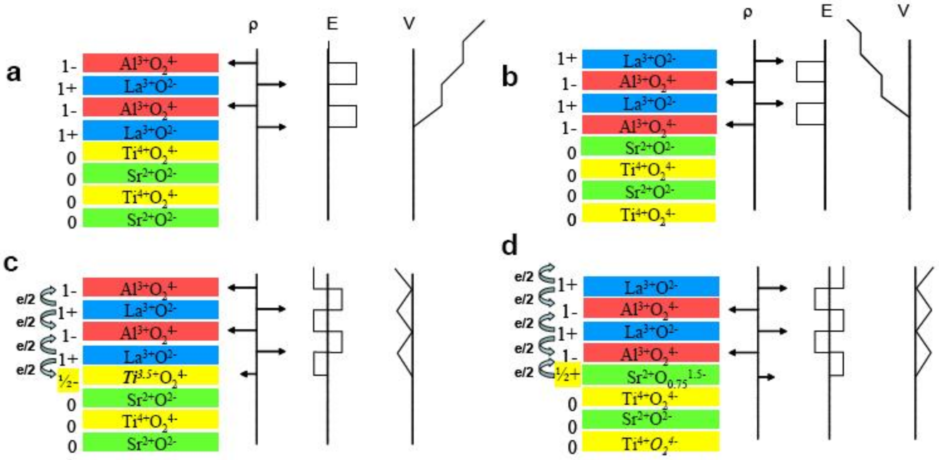

Figure 2.3 Interfaces of $SrTiO_3$ and $LaAlO_3$.[12] The net charge (ρ), electric field (E) and potential (V) are shown. In the absence of electronic reconstruction (a and b), the net charge distribution leads to a potential build up. After reconstruction (c and d), the polar catastrophe is resolved.

The electronic reconstruction at the $SrTiO_3/LaAlO_3$ interface is schematically shown in figure 2.3. If the interface plane consists of TiO_2/LaO, 0.5 electron per unit cell is theoretically donated to the last Ti layer, avoiding the polar catastrophe. On the other hand, if the interface consists of a SrO/AlO_2 plane, the polar catastrophe is avoided by theoretically removing 0.5 electron per unit cell.

2.3 Electronic transport properties of interfaces

Since the discovery of a high mobility two-dimensional electron gas at the $SrTiO_3/LaAlO_3$ interface[4], the electronic properties of this interface have been intensively investigated. The electronic transport properties of the interface appear to be strongly influenced by surface termination and deposition parameters. A framework of some of these parameters which are also interesting for the research of these interfaces grown on different substrates, is given in the remainder of this section.

2.3.1 Influence of surface termination

As already pointed out in section 2.2, depending on the surface termination of the $SrTiO_3$, different interface configurations are possible. For the extreme case of single termination, the interface is either conducting or insulating. The TiO_2 terminated surface shows metallic behavior down to low temperatures, while the SrO terminated surface shows insulating behavior and cannot be accurately measured at low temperatures. These two extreme cases are called n-type and p-type interfaces, respectively. An example of the difference in temperature dependence of the resistance for the two interface configurations is shown in figure 2.4

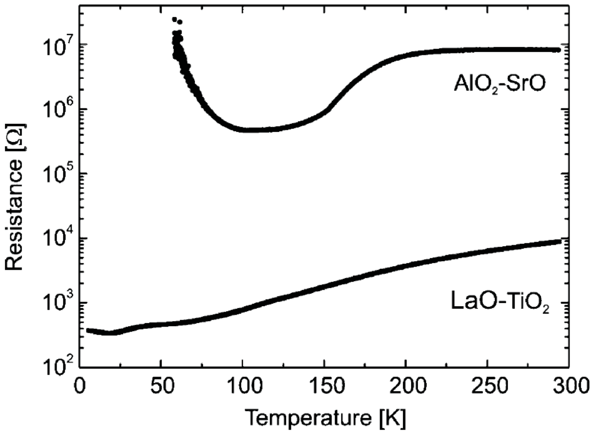

Figure 2.4 Difference in temperature dependence of the sheet resistance for a SrO and a TiO_2 terminated $SrTiO_3$ surface. Samples were grown at a temperature of 850 °C and $3 \cdot 10^{-5}$ mbar oxygen pressure. A 26 unit cells thick $LaAlO_3$ film was deposited. [6]

The difference between the two extreme interface configurations was determined by Ohtomo and Wang[4], and investigated in more detail by Nishimura et al.[13] For different SrO coverage on a TiO_2 terminated surface, a 13 monolayer thick $LaAlO_3$ film was deposited. Sheet carrier density, sheet resistance and sheet carrier mobility were determined as a function of SrO coverage of the surface, as shown in figure 2.5. Starting with an electron density of 0.5 electrons per Ti site, this value decreases to zero for a full SrO coverage. Additionally, the increase in SrO coverage leads to an increase of the sheet resistance. For the carrier mobility no systematic change could be observed, all samples showed comparable carrier mobilities.

2.3.2 Pressure dependence

For TiO_2 terminated surfaces, the partial oxygen pressure dependence during deposition was investigated by Ohtomo and Wang, Thiel et al. and by Brinkman et al.[4, 14, 15] The sheet resistance for different oxygen pressures are shown in figure 2.6. A lower oxygen pressure clearly leads to a lower sheet resistance. For deposition pressures between 10^{-4} and 10^{-5} mbar superconductivity is measured below 200 mK[16], while for deposition pressures in the 10^{-3} mbar range, magnetic effects are measured.[6]

Deposition at very low oxygen pressures (10^{-6}), leads to unusual high carrier densities and high mobilities.[4] This can only be explained by including the role of oxygen vacancies in the

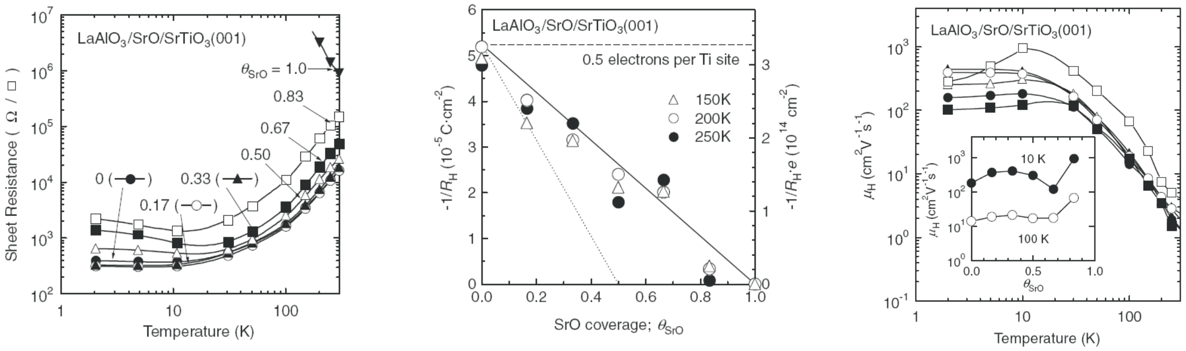

Figure 2.5 Left: temperature dependence of the sheet resistance for different SrO coverage. Middle: sheet carrier density as a function of SrO coverage. Carrier density decreases for increasing SrO coverage, and abruptly changes from 0.83ML SrO coverage. Right: temperature dependence of the charge carrier mobility for different SrO coverage. No systematic change can be observed, indicating that the sheet resistance is mainly determined by the sheet carrier density. [13]

top layer of the $SrTiO_3$ substrate. At these low pressures, defects will appear at the interface due to irradiation damage. The arriving species will create oxygen vacancies at the surface of the $SrTiO_3$, because of their high kinetic energy. By changing the valence of a Ti-atom from 4+ to 3+, such an oxygen vacancy can be easily formed. While the effect is still present in samples grown at higher oxygen pressures, it is much weaker. For increasing deposition pressures, the contribution of oxygen vacancies in $SrTiO_3$ reduces and the interface conductivity becomes the dominant contribution.[6]

2.3.3 Thickness of the $LaAlO_3$ layer

A detailed study about the influence of the thickness of the $LaAlO_3$ layer for ultrathin films was performed by Thiel et. al.[17] Samples were grown with a thickness up to 15 unit cells. A sharp transition from insulating to conducting behavior is observed at a critical thickness of 4 unit cells. Below this thickness, the conductivity was below the measurement limit and no sheet carrier density could be determined. However, for thicknesses of 4 unit cells and more, the sheet conductivity and sheet carrier density were constant and independent of thickness. These results are shown in figure 2.7.

2.3.4 Resistivity anisotropy

Assuming that the interface conductivity is 2-dimensional, electron scattering will be largely determined by the step and terrace structure at the interface. This will presumably lead to an anisotropy of the interface resistance, corresponding to the miscut direction. Some indications of this anisotropy were observed by Huijben.[9] Several samples were structured with transport geometries under different angles. For single TiO_2 terminated surfaces no anisotropy was measured at all. However for a partially SrO covered surface, some differences in resistances were measured. Although no clear anisotropy could be determined, two peaks were measured, which roughly corresponded to the miscut direction.

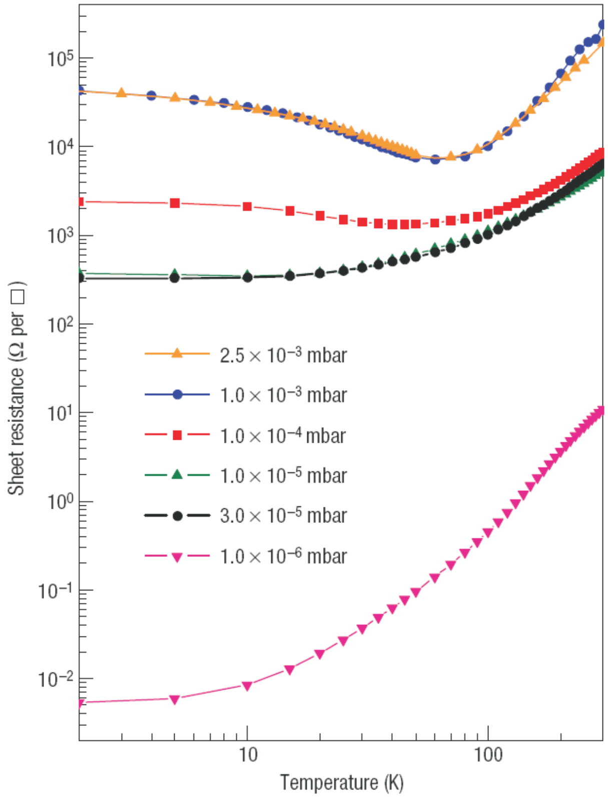

Figure 2.6 Sheet resistance of n-type $SrTiO_3$/$LaAlO_3$ conducting interfaces. Temperature dependence of the sheet resistance for samples grown at different partial oxygen pressures. [15]

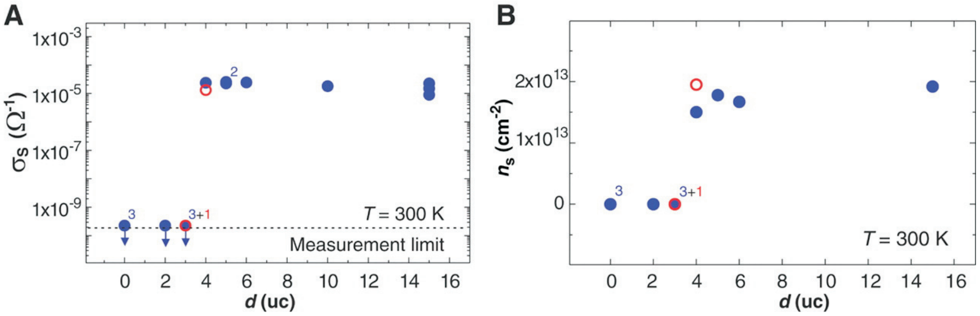

Figure 2.7 Sheet conductivity and sheet carrier density as a function of the thickness of the $LaAlO_3$ layer. The blue dots denote samples grown at 770 °C, while the red dots denote samples grown at 815 °C. Measurements were performed at 300 K. The numbers indicate the number of samples that yielded the same result. [17]

Chapter 3

Substrates

As described in chapter 1, instead of $SrTiO_3$, a different substrate material is used for this research. The first section of this chapter gives a description of the choice of a suitable substrate. In the last section, the developed substrate treatment is discussed.

3.1 Substrate choice

Within the class of perovskites, several substrates are commercially available. For this research, important properties of the substrate are the crystal structure, the lattice parameter and the electronic properties. To reduce effects from stress and strain of the $SrTiO_3$ layer, the substrate of choice has preferably a cubic crystal structure and a lattice constant close to that of $SrTiO_3$ (3.905 Å). In addition, the substrate should be electrically insulating. Preferably, the substrate remains insulating after argon ion etching during structuring of the sample into various measurement geometries.

Possible candidates for substrates are given in table 3.1. For clarity, $SrTiO_3$ and $LaAlO_3$ are also included in this table and the substrates are ordered with increasing (pseudo) cubic in-plane lattice constant. From these substrates, $LaSrAlTaO_3$, with the composition $(LaAlO_3)_{0,3}(Sr_2AlTaO_6)_{0,7}$, is chosen as the best suitable substrate. The crystal has a cubic structure and the lattice constant closely matches $SrTiO_3$ (and $LaAlO_3$). Moreover, $LaSrAlTaO_3$ is electrically insulating, also after argon ion etching.

3.2 $LaSrAlTaO_3$ substrate treatment

The quality of thin films strongly depends on the quality of the substrate on which they are deposited. Although polished substrates are commercially available, careful substrate treatment is necessary to obtain an atomically smooth surface. Only a few publications about $LaSrAlTaO_3$ substrates can be found[23, 24, 25] and no standard substrate treatment is available. Because of the complex composition of the material, a single terminated surface is most likely difficult to achieve. However, it should be possible to obtain an atomically flat surface with a well defined step and terrace structure, by an annealing procedure. This section describes the developed annealing procedure for $LaSrAlTaO_3$ substrates, leading to a well defined step and terrace structure.

Before annealing, the substrates are cleaned in ethanol and acetone in an ultrasonic bath for a minimum of 5 minutes. An atomic force microscopy image of an as-received substrate is shown

Table 3.1 Possible substrate candidates [18, 19, 20, 21, 22]

Material	**Orientation**	**Structure**	**Lattice constants**	**(Pseudo) Cubic in-plane Lattice Constant**
$LiGaO_2$	(100), (001), (111)	Orthorombic	$a = 0.541\,nm$, $b = 0.501\,nm$, $c = 0.638\,nm$	$0.318\,nm$
$YAlO_3$	(100), (110), (111)	Orthorombic	$a = 0.518\,nm$, $b = 0.531\,nm$, $c = 0.735\,nm$	$0.372\,nm$
$SrLaAlO_4$	(100), (001), (110)	Tetragonal	$a = 0.375\,nm$, $c = 1.263\,nm$	$0.375\,nm$
$LaAlO_3$	(100), (110), (111)	Cubic	$a = 0.382\,nm$	$0.382\,nm$
$SrLaGaO_4$	(100), (001), (110)	Tetragonal	$a = 0.384\,nm$, $c = 1.268\,nm$	$0.384\,nm$
$\mathrm{NdGaO_3}$	(110), (100), (001)	Orthorombic	$a = 0.543\,nm$, $b = 0.550\,nm$, $c = 0.771\,nm$	$0.386\,nm$
$(LaAlO_3)_{0,3}(Sr_2AlTaO_6)_{0,7}$ ($\mathrm{LaSrAlTaO_3}$)	(100), (110), (111)	Cubic	$a = 0.387\,nm$	$0.387\,nm$
$SrTiO_3$	(100), (110), (111)	Cubic	$a = 0.391\,nm$	$0.391\,nm$
$DyScO_3$	(110)	Orthorombic	$a = 0.554\,nm$, $b = 0.571\,nm$, $c = 0.789\,nm$	$0.394\,nm$
$GdScO_3$	(110)	Orthorombic	$a = 0.545\,nm$, $b = 0.575\,nm$, $c = 0.793\,nm$	$0.396\,nm$
MgO	(100), (110), (111)	Cubic	$a = 0.421\,nm$	$0.421\,nm$
$LiAlO_2$	(100), (001), (111)	Tetragonal	$a = 0.517\,nm$, $c = 0.626\,nm$	$0.517\,nm$
$MgAl_2O_4$ (Spinel)	(100), (110), (111)	Cubic	$a = 0.809\,nm$	$0.809\,nm$
$\mathrm{Y}_3Al_5O_{12}$	(100), (110), (111)	Cubic	$a = 1.20\,nm$	$1.20\,nm$
$Gd_3Ga_5O_12$	(100), (110), (111)	Cubic	$a = 1.238\,nm$	$1.238\,nm$

in figure 3.1. As a start, an annealing temperature of 1050 °C was used. To exclude differences between substrates, the same substrate was annealed several times with increasing anneal times. The substrate was annealed in an oxygen flow of 150 ml/min and the ramp rate of the oven was switched off. After each anneal step, the surface was investigated by atomic force microscopy.

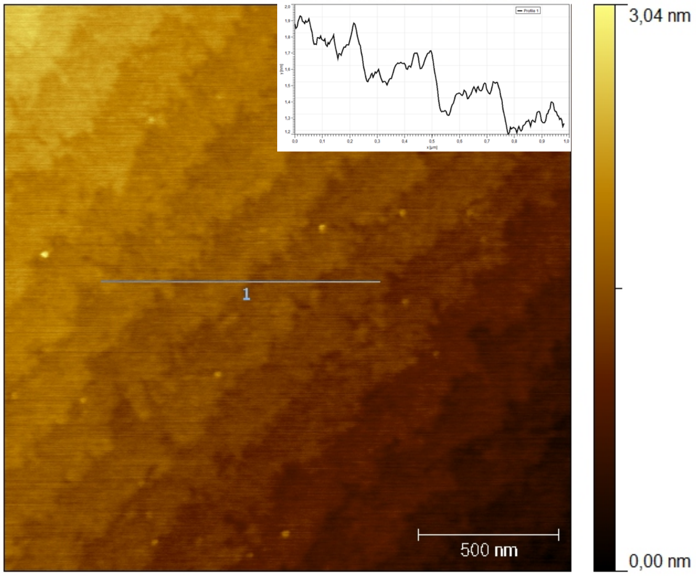

Figure 3.1 AFM image of an LaSrAlTaO$_3$ substrate as-received. The surface topography and the line profile (inset) are shown.

Before annealing, the step and terrace structure on the surface is already clearly visible (figure 3.1). However, the step edges are not well-defined and the surface roughness on the terraces is relatively high. Already after one annealing step of 2 hours (figure 3.2), the roughness on the terraces decreases. An additional annealing step of 2 hours leads to a further decrease of the surface roughness and relatively straight step edges (figure 3.3(a)). After three anneal steps of each 2 hours, minimal roughness is measured on the terraces and the steps are well defined (figure 3.3(b)). The extracted profile indeed shows sharp step edges of approximately 0.4 nm. This step height corresponds to single unit cell steps (0.387 nm), suggesting that the surface has either single A or B site termination. Although the surface morphology on the terraces has been improved, the step edges are still meandering and are not straightened out.

In an attempt to decrease this meandering, the substrate was annealed for an additional 6 hours (figure 3.3(c)). After this annealing step, the height of the step edges was reduced to approximately 0.2 nm, corresponding to half unit-cell steps (0.1935 nm). The creation of half-unit cell steps indicates that material diffuses towards the surface, which is possibly the start of a termination switch. A last annealing procedure of 24 hours was performed (figure 3.3(d)) to see if again single unit-cell steps could be created. Indeed single unit cell step heights were measured in the profile. However, clusters were found at the surface. Diffusion towards the surface possibly led to enrichment and clustering of one or two elements at the surface. Comparing the shape of the step edges from figures 3.3(b) and 3.3(d), it is clear that the meandering of the step edges is different. This difference, in combination with the observation of half-unit cell steps in between the two anneal steps, could indicate that the termination has switched from A-site to B-site or

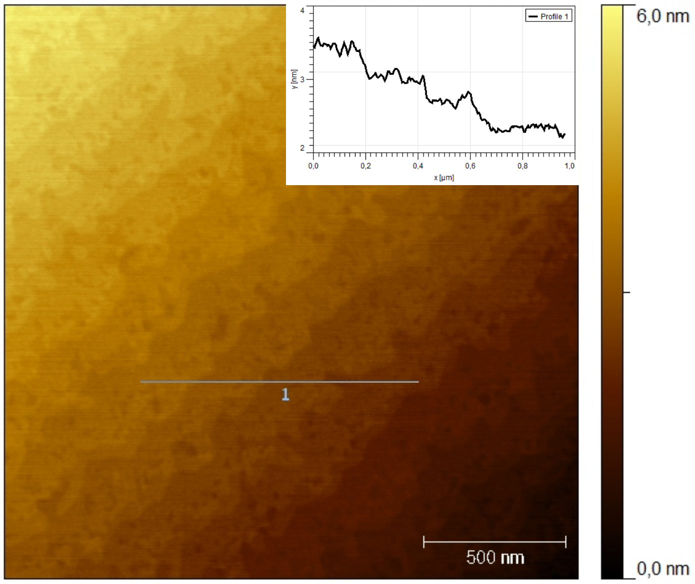

Figure 3.2 AFM image of an LaSrAlTaO$_3$ substrate after annealing for 2 hours. The surface topography and a line profile (inset) are shown.

vice versa.

Taking into account that also some annealing already takes place during heating and cooling, most substrates used for this research were annealed for 10 hours. This yielded comparable results as shown in figure 3.3(b). However, for some substrates a combination of single unit-cell steps and half unit-cell steps was observed, indicating both A and B site termination. In order to determine the optimal annealing time, the miscut angle of the substrate should also be taken into account.

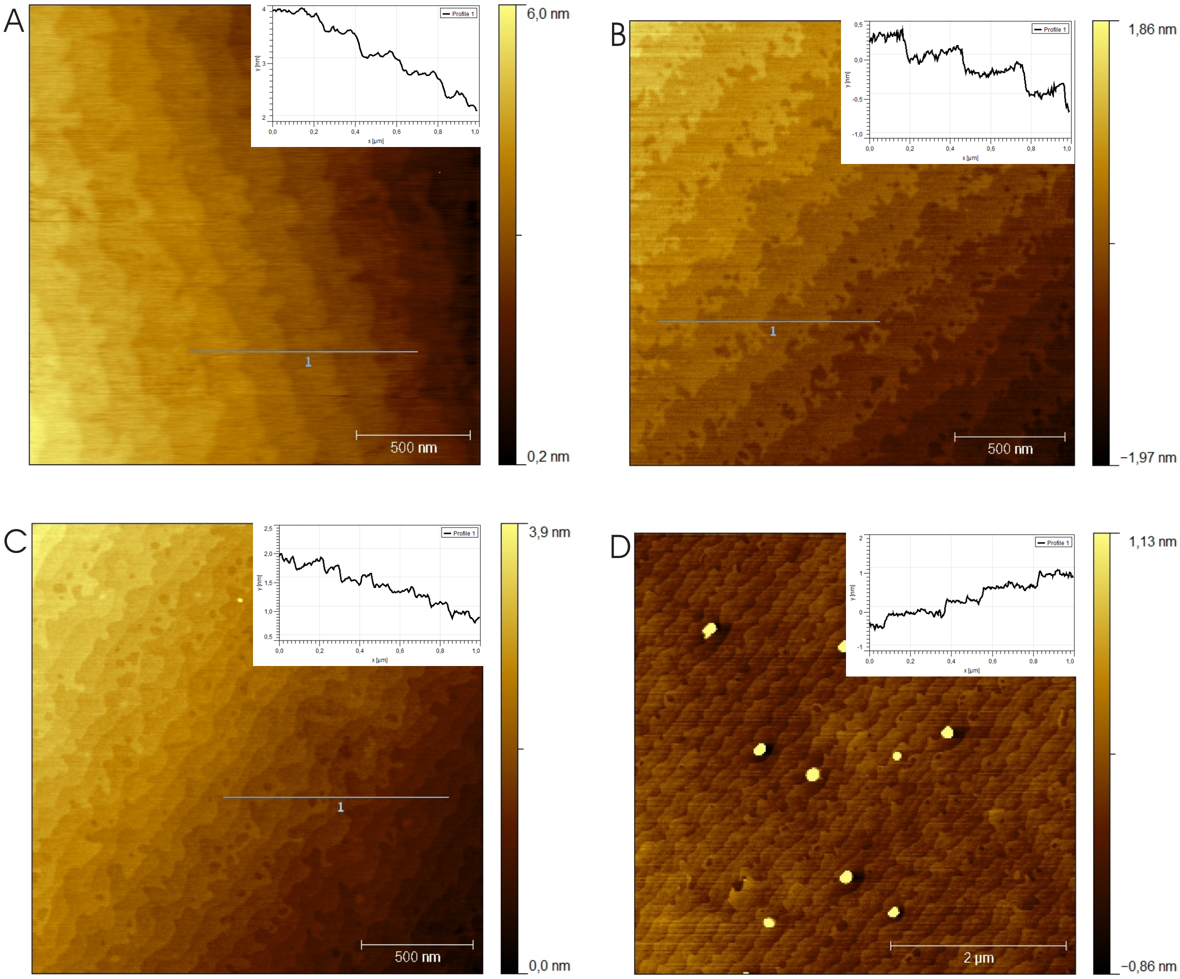

Figure 3.3 AFM images of subsequent anneal steps at a temperature of 1050 °C. For all anneal steps, the surface topography is shown and a line profile is shown in the inset. Left top is after two anneal steps, leading to a total annealing time of 4 hours. Right top is after three anneal steps with a total time of 6 hours. Left bottom is after four anneal steps with a total time of 12 hours. Right bottom is after five anneal steps with a total time of 36 hours. Note the different scan size of the last image, to show the formed clusters. The line scan shown in the inset of this image was taken from scan with a smaller scan size.

Chapter 4

Sample Fabrication and Characterization

The process of fabrication and characterization of samples is described in this chapter. Samples are fabricated by pulsed laser deposition and characterized by atomic force microscopy and X-ray diffraction. For these techniques, first a general introduction is given. Subsequently, the result for the $SrTiO_3/LaAlO_3$ heterostructures on $LaSrAlTaO_3$ substrates is given. After structural characterization, the electronic properties of the samples are studied. A description of the techniques and some results are given in section 4.3

4.1 Pulsed Laser Deposition

Pulsed laser deposition is a physical vapor deposition technique often used for the growth of (complex) oxide materials. The technique makes use of a highly energetic pulsed laser to ablate material from a target. In order to obtain sufficiently high energy densities at the target, the laser beam is focused by an external lens. The heated material at the target quickly evaporates and during the remainder of the laser pulse it will be heated even more in order to form a plasma plume. The plasma plume expands away from the target (towards the substrate) due to the pressure gradient. The material will adsorb at the substrate and will form a thin layer after undergoing a thermally-activated diffusion process.[26]

The process is schematically shown in figure 4.1. The incoming laser beam hits the selected target under an angle of 45°. The sample is mounted on a heater block and is placed right in front of the target stage. At this position the most homogeneous part of the plasma plume will arrive at the sample. The target stage consists of a rotating carousel, providing the possibility to use multiple target materials during deposition.

Important parameters for the pulsed laser deposition process are laser fluency, laser spot size at the target, target-to-substrate distance, background gas pressure, background gas composition and the substrate temperature. The combination of these parameters provide the possibility to tune the deposition process. The supersaturation during the deposition pulse, subsequently relaxation on the substrate and the kinetics of the species arriving on the substrate can all be controlled by adjusting the parameters.

Because of the pulsed nature of the pulsed laser deposition process, adsorption and diffusion of the arriving species can occur at two different time scales. During one single pulse, about

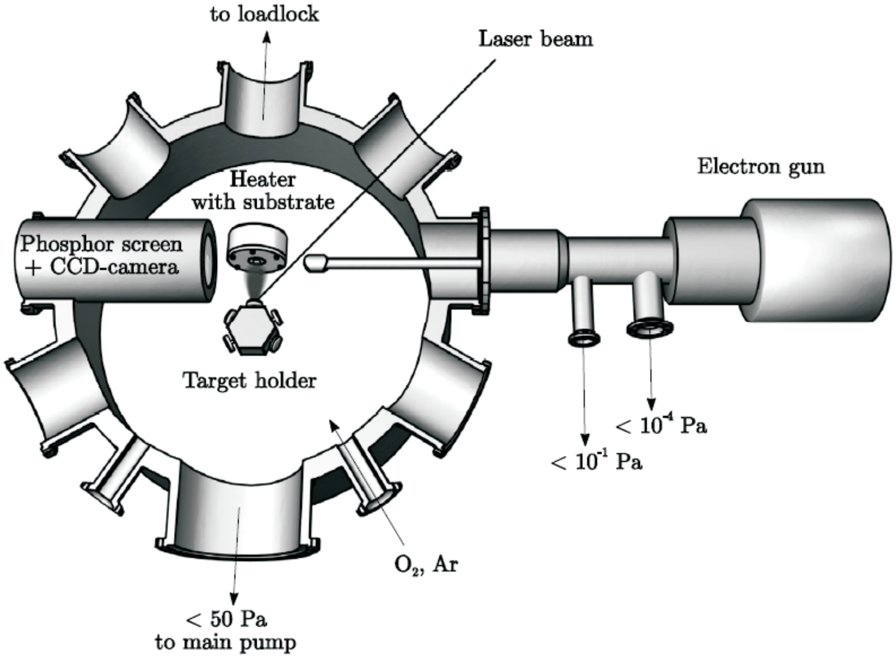

Figure 4.1 Schematic overview of a typical pulsed laser deposition setup [9]

$3 \cdot 10^{13}$ ion species arrive at the substrate. The typical overall growth rate is 0.2 nm/s which is comparable to other deposition techniques, such as molecular-beam epitaxy. However, the material is only deposited during the short plasma pulse durations (which are typically 500 $\mu s^{[27]}$), leading to much higher species density during the actual deposition. This high density causes a high nucleation density. Because the mean diffusion time exceeds the plasma pulse duration, adatoms diffuse across the surface and find their optimal positions in between the plasma pulses. This relaxation can be observed with REED during growth. The high nucleation density and the possibility for diffusion during growth favor layer-by-layer growth. The interplay of the supersaturation and subsequent relaxation determines the growth properties and can be tuned by adjusting the growth parameters.[5]

The samples were grown on a pulsed laser deposition setup with a KrF excimer laser (Lambda Physik LPX 210) with a wavelength of 248 nm. The repetition rate can be varied between 1 Hz and 100 Hz and the maximum pulse energy is 1 J. The duration of a laser pulse is 25 ns. The pressure in the system can be controlled by two valves and a mass flow (0-40 ml/min), which results in stable deposition pressures from $1 \cdot 10^{-6}$ $mbar$ up to $3 \cdot 10^{-1}$ $mbar$. For the background gas, only oxygen was used. To maintain a homogeneous spot on the target, a mask was placed in the center of the laser beam outside the vacuum system. To obtain high energy densities at the target surface, a lens is placed in the laser beam. During deposition the target is scanned in horizontal direction, to spread wear of the target. The sample is loaded on a substrate holder with heater through a loadlock. The heater can be heated up to 950 °C, and the temperature is measured with a K-type thermocouple. The deposition parameters used for the deposition of $SrTiO_3$ and $LaAlO_3$ are given in table 4.1.[9]

Table 4.1 Deposition parameters for $SrTiO_3$ and $LaAlO_3$

Material	STO	LAO
Laser Fluence	$1,3\,J/cm^2$	$1,3\,J/cm^2$
Laser Repetition Rate	$1\,Hz$	$1\,Hz$
Mask Position	$1536\,mm$	$1536\,mm$
Mask Size	$30\ mm^2$	$30\ mm^2$
Lens Position	$642\,mm$	$642\,mm$
Target-Substrate Distance	$56\,mm$	$56\,mm$
Temperature	$850\,°C$	$850\,°C$
Pressure	$1 \cdot 10^{-1}\,mbar$	$1 \cdot 10^{-6} - 1 \cdot 10^{-4}\,mbar$
Deposition Rate	$25\,pulses/ML$	$17\,pulses/ML$

4.1.1 RHEED

Reflection High Energy Electron Diffraction (RHEED) is a surface sensitive technique that can be used to study surface properties during growth. High energy electrons of $10-35\ keV$ are incident on the surface at a grazing angle, typically 1° to 5°.Because of the grazing angle of incidence, the electrons only interact with the top few layers of materials, making RHEED a surface sensitive technique. Due to the grazing angle of incidence, the technique can be used during pulsed laser deposition without any interference. The setup of a RHEED system in a pulsed laser deposition setup is schematically shown in figure 4.2.

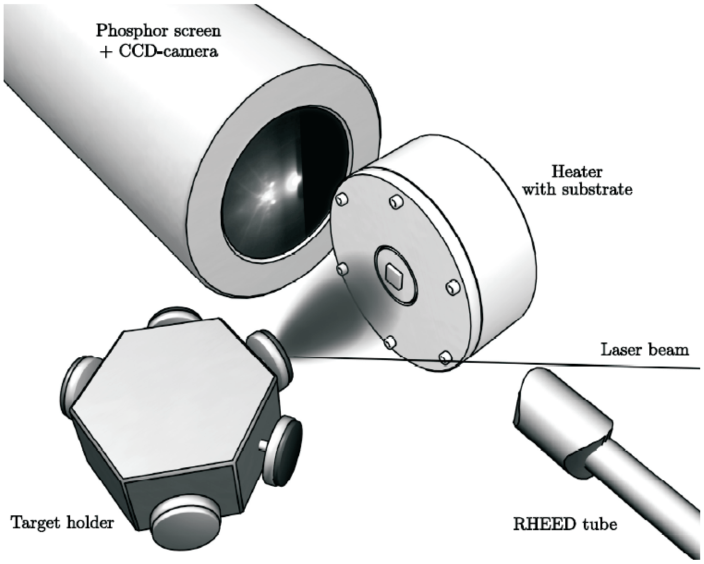

Figure 4.2 RHEED monitoring during pulsed laser deposition process [9]

By looking at the diffraction pattern, information about the surface of the sample can be obtained. If the surface is atomically flat, the diffraction pattern will show sharp diffraction spots lying on concentric circles (Laue circles). While in the other extreme case of three dimensional features at the surface of the sample, a rectangular pattern of spots will be observed. The growth can be monitored closely by recording the peak intensity of the specular spot during deposition.

In the case of layer-by-layer growth, one can observe oscillations that correspond to the deposition of monolayers of material. This principle is shown in figure 4.3, where the growth of 10 ML of $SrTiO_3$ and 10 ML of LAO is shown. When material is deposited (which leads to a roughened surface), the intensity decreases. A minimum intensity is observed when exactly 0.5 monolayer is deposited. From this point, the intensity increases again to reach a maximum when a single monolayer is deposited.

Before deposition, the diffraction spot of the substrate is recorded. The substrates usually show sharp diffraction spots (see figure 4.3), indicating a flat surface. The intensity oscillations during the growth of a 10 ML $SrTiO_3$ film (figure 4.3) suggest smooth layer-by-layer growth. This is confirmed by the diffraction spots after deposition, shown in figure 4.3. The diffraction spots are still sharp spots without any 3-d spots. The intensity oscillations for the subsequent deposition of a 10 ML $LaAlO_3$ film are also shown in figure 4.3. Again, oscillations can be clearly observed. Judging from the diffraction spots (figure 4.3), which are not as sharp as before deposition, the surface roughness is probably slightly increased.

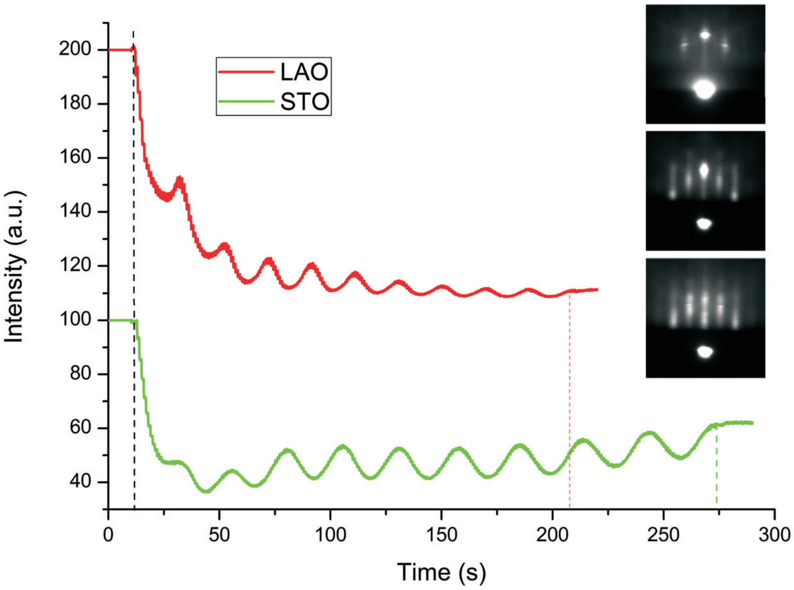

Figure 4.3 RHEED measurements during deposition of 10 ML STO and 10 ML of LAO. Deposition at "standard" settings (see table 4.1 and a deposition pressure of $5 \cdot 10^{-6}$ *mbar*. The intensity oscillations during deposition of $SrTiO_3$ and $LaAlO_3$ are shown. RHEED data is shifted for clarity. At the right, the diffraction patterns before deposition (top), after $SrTiO_3$ deposition (middle) and after $LaAlO_3$ deposition (bottom) are shown.

4.2 Thin film structural characterization

After growth of the samples, the structural and surface properties of the samples were investigated. In this section the most important characterization techniques, X-ray diffraction and atomic force microscopy and some typical results, will be shortly explained. A short explanation of the used setups will also be given.

4.2.1 X-Ray Diffraction

X-ray diffraction is a powerful tool to investigate the structural properties of a sample. A typical X-ray diffraction setup is schematically shown in figure 4.4. The sample is placed on a chuck and the positions of both the incoming X-ray beam and the X-ray detector with respect to the sample, can be controlled with great precision. A variety of scans can be performed by a typical diffractometer. The different types of scans can be divided into crystallographic and optical scans. Some short remarks about these two types of scans will be made in this section. Additionally, at the end it will become clear why the possibility to obtain information about the optical surface and layer roughness, as well as the crystallographic properties of the sample makes this technique especially interesting.

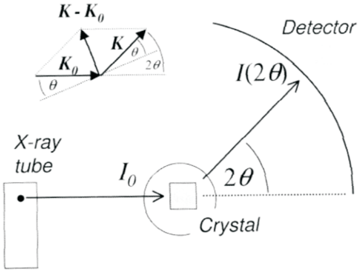

Figure 4.4 Typical X-ray diffraction setup

Several crystallographic properties can be determined with X-ray diffraction by making use of the periodicity of the crystal. For the research described in this report, only basic scans such as a θ and a $2\theta\backslash\omega$ scan were performed. The θ scan, also called rocking curve, is a scan of θ around Bragg conditions:

$$\lambda = 2d\sin\theta \tag{4.1}$$

with λ the wavelength of the X-rays, d the spacing between the crystallographic planes and θ the angle between the incoming X-rays and the sample. The width of this peak provides information about the crystal quality of the sample. The $2\theta\backslash\omega$ scan, is a scan of the angle 2θ, while the angle ω is varied accordingly, such that $\omega = \theta$ during the scan. This scan provides information about the lattice constants of the sample. One can for example determine the out-of-plane lattice constant (of the substrate and the grown layers) by aligning on one of the (00x) planes. It is also possible to determine the direction of the in-plane crystal axis, by alignment on a plane with an additional in-plane component. This can be done by performing a ϕ scan around Bragg conditions. The recorded maxima will then correspond to the directions of the in-plane crystal axis.

Rather than making use of the periodicity of the crystal, one can also use reflectivity to determine film properties. This can be done by performing a $2\theta\backslash\omega$ scan for small angles, after alignment of the sample at the optical surface. The result of this low-angle reflectivity scan, can be used to determine the layer thickness and roughness of the different layers of the sample. An example of such a scan is shown in figure 4.5.

When the results of crystallographic and optical surface scans are combined, additional information can be obtained. The difference in alignment of the ξ and ζ axes, for the (out-of-plane)

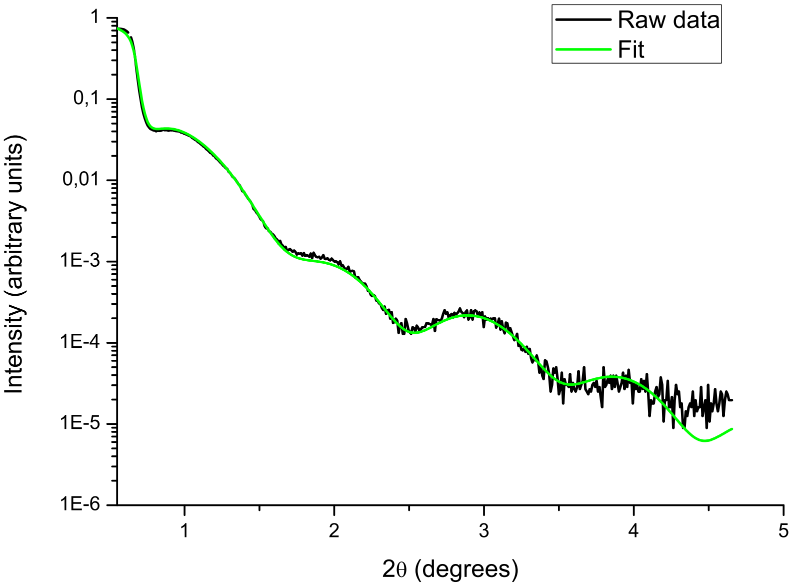

Figure 4.5 Reflectivity scan of a sample with 10 ML of STO and LAO. The fit results confirmed layer thicknesses. A surface roughness of approximately one unit cell height was calculated from the fit results, which is confirmed by atomic force microscopy. A slightly higher $SrTiO_3/LaAlO_3$ interface roughness of 1.5 unit cells was calculated.

crystal axis and the optical surface, is determined by the miscut angle and direction of the substrate. From the 2 different sets of values for ξ and ζ, the miscut angle and direction can be determined. Because the measurement is performed over a relatively large area of the sample (approximately 1 mm), this method provides a mean value of the sample.

All X-ray diffraction measurements were performed on a Bruker D8 diffractometer, with a high-flux-Kα-1 radiation source, with a wavelength of 1.54058 Å. The optional $\zeta\backslash\xi$ tilt stage was used for alignment of the crystal and optical axes. In order to optimize the alignment, a detector slit with a width of 0.1 mm was mainly used.

4.2.2 Atomic Force Microscopy

Atomic force microscopy is a versatile analysis technique, which can be used to determine a variety of surface characteristics. For the work described in this report, atomic force microscopy was mainly used to determine the surface topography. However, also friction and phase contrast were used to some extent.

Measuring surface topography is usually done by either contact mode (CM) or tapping mode (TM) atomic force microscopy. In contact mode, the sharp tip is gently brought into contact with the surface. By measuring the deflection of the tip (usually with an optical method), the surface topography can be determined. In tapping mode, the tip is brought close to the surface (usually within tens to hundreds of Ångströms). The tip is then set to oscillate at a frequency in the range of 100 kHz to 400 kHz and by recording changes in vibrational amplitude or resonant frequency, the surface topography can be reconstructed.[28] To obtain information about the surface termination of samples, phase imaging was also used during TM atomic force microscopy. This phase imaging method records the phase shift between the oscillating cantilever and its piezodriver. Phase imaging can be used to obtain information about surface properties such as composition and friction, rather than height differences.[29]

Atomic force microscopy measurements were done on a Veeco Dimension Icon AFM and a Veeco Multimode SPM. The measurements were performed ex-situ and at room temperature. For most measurements, tapping mode was used. This imaging mode gives accurate information about the surface topography. The roughness of the surface can be determined and the observed step and terrace structure also gives an indication about the miscut angle and direction of the sample.

For the surface analysis of thin films, the surface morphology of the sample after growth is compared with that of the substrate. An example of this is shown in figure 4.6. The substrate was annealed for 10 hours at a temperature of $1050\,^{\circ}C$. After atomic force microscopy, 10 ML of $SrTiO_3$ and 10 ML of $LaAlO_3$ were deposited. After deposition the step edges can still be clearly observed, although the surface roughness has increased somewhat.

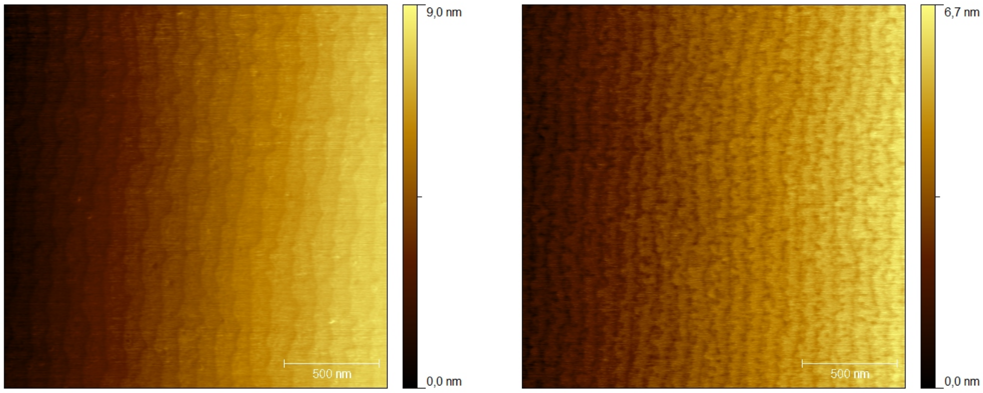

Figure 4.6 AFM images of the annealed $LaSrAlTaO_3$ substrate before deposition (left) and of the final heterostructure (right). 10 ML of $SrTiO_3$ and 10 ML of $LaAlO_3$ were deposited at standard deposition parameters (table 4.1) and a deposition pressure of $3 \cdot 10^{-5}$ *mbar* for the $LaAlO_3$ layer.

4.3 Electronic transport analysis

4.3.1 Resistance measurements

To investigate the resistance of the $SrTiO_3/LaAlO_3$ interfaces, several measurement geometries were used. By measuring the resistance at different angles across the sample, the anisotropy of the resistance can also be determined. These measurements can be expanded with temperature dependent measurements to study the resistance behavior in more detail. For all resistance measurements, 4-point contact measurements were used which eliminates any contributions from contact resistances.

As a first test, some samples were measured without structuring the sample. The wirebonds were placed directly on the corners and the middle of the sides. The resistance can be measured for 4 different directions and this already provides information about the anisotropy and the temperature dependence of the resistance. From these measurements a large anisotropy was observed.

In order to study the observed anisotropy of the resistance in more detail, a different measurement geometry was used. Although several masks were already available for these measurements, a new mask design was made. This new mask design was made such that the measurement geometries are relatively small and placed central on the sample, to minimize any inaccuracies as a consequence of inhomogeneities throughout the sample. The layout of the measurement geometry is shown in figure 4.7.

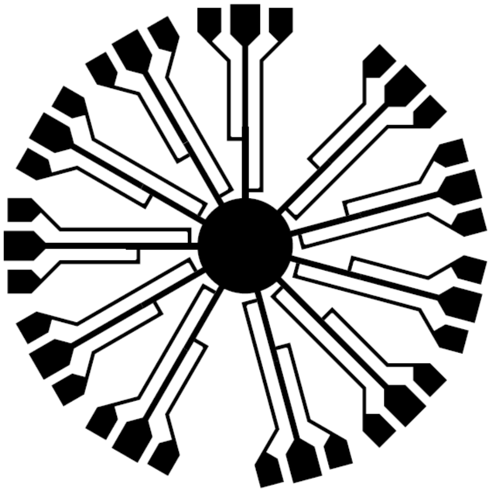

Figure 4.7 Measuring geometry for anisotropy measurements

In practice this structure provided good results. Anisotropy measurements were performed at different temperatures. The temperature dependence for different angles of one of the samples is shown in figure 4.8. The determined anisotropy at room temperature is shown in figure 4.9(a). The result was fitted with a sine function. The crystal axes and step and terrace structure (miscut direction) were determined as possible origin of the anisotropy. Because both of these have a periodicity of 90 ° and have the same direction for this sample, the two cannot be distinguished.

By combining the resistance versus temperature curves for the different angles, the anisotropy at different temperatures can also be determined, as shown in figure 4.9(b). The curves were fitted with a sine function with a period of 90 °. The anisotropy dramatically increases for a temperature of 5 K due to the difference in temperature dependence of the different angles. This is also shown in table 4.2, where the amplitude, offset (mean value) and relative amplitude ($\frac{Amplitude}{Offset}$) are given to compare the results for different temperatures.

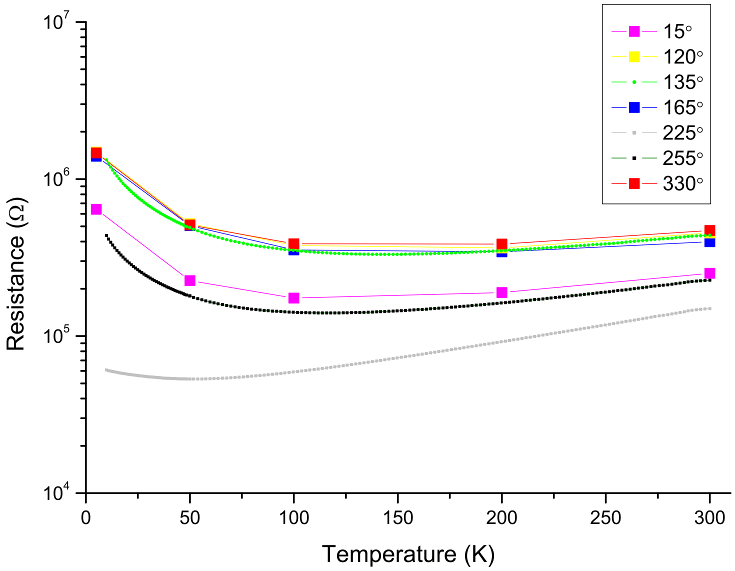

Figure 4.8 Temperature dependence of the resistance for different directions. Measurements were performed on a sample with 10 ML of $SrTiO_3$ and 10 ML of $LaAlO_3$ deposited at standard deposition settings (table 4.1 and a pressure of 10^{-5} *mbar* for the $LaAlO_3$ layer.

Table 4.2 Fit results for different temperatures for a sample with 10 ML of $SrTiO_3$ and 10 ML of $LaAlO_3$ deposited at standard deposition settings (table 4.1 and a pressure of 10^{-5} *mbar* for the $LaAlO_3$ layer.

Temperature	Amplitude	Offset	$\frac{Amplitude}{Offset}$
$300\,K$	$1.6 \cdot 10^5$	$3.2 \cdot 10^5$	0.51
$200\,K$	$1.5 \cdot 10^5$	$2.4 \cdot 10^5$	0.60
$100\,K$	$1.7 \cdot 10^5$	$2.3 \cdot 10^5$	0.71
$50\,K$	$2.2 \cdot 10^5$	$3.2 \cdot 10^5$	0.69
$5\,K$	$7.2 \cdot 10^5$	$8.4 \cdot 10^5$	0.86

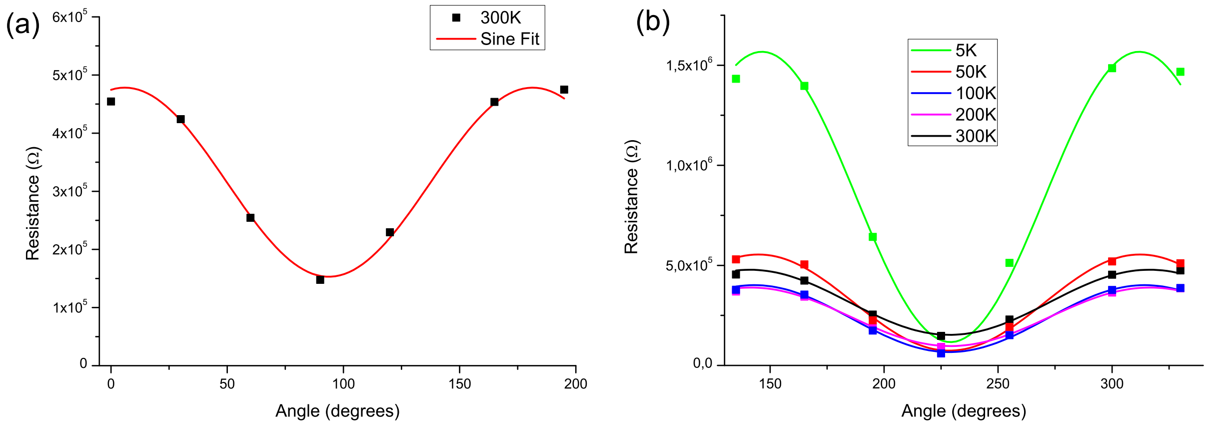

Figure 4.9 Anisotropy at a temperature of 300 *K* (a) and various temperatures (b). The data was fitted with a sine function with a period of 90 °. Measurements were performed on a sample with 10 ML of $SrTiO_3$ and 10 ML of $LaAlO_3$ deposited at standard deposition settings (table 4.1 and a pressure of 10^{-5} *mbar* for the $LaAlO_3$ layer.

4.3.2 Hall effect measurements

In addition to the resistance measurements, hall effect measurements were performed. The basic measurement geometry of a Hall measurement is shown in figure 4.10. A current is applied and an external magnetic field is applied normal to this current as indicated. The Lorentz force causes a shift of the electrons in a direction perpendicular to the magnetic field and the current. This movement of the charge carriers leads to an electric field, which is measured as U_H.

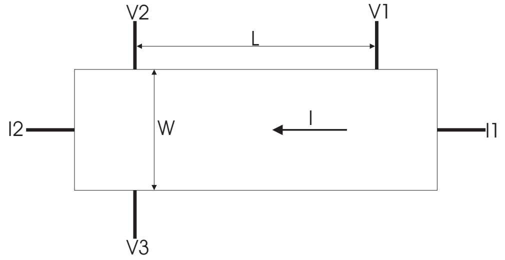

Figure 4.10 Hall bar geometry used for Hall effect measurements. The two current contacts (I1 and I2) are connected so the direction of the current is as indicated. The longitudinal resistance can be measured by the voltage contacts V1 and V2. The Hall voltage is measured with the voltage contacts V2 and V3.

Assuming equilibrium, the net force on the charge carriers equals zero:

$$F_y = -e(v \times \mathbf{B})_{\mathbf{y}} - \mathbf{e}\xi_{\mathbf{y}} = \mathbf{e}\mathbf{v}_{\mathbf{x}}\mathbf{B} - \mathbf{e}\xi_{\mathbf{y}} = \mathbf{0}, \tag{4.2}$$

with v_x the the velocity of the charge carriers in the x-direction and $\xi_y = U_H/b$ the Hall-field. Assuming that the current is only carried by electrons, the current density is given by:

$$j_x = \frac{I}{bd} = -nev_x \Rightarrow v_x = \frac{-I}{nebd}, \tag{4.3}$$

with n the electron concentration. From these equations it follows immediately that:

$$\frac{U_H}{b} = B(\frac{-I}{nebd}) \Rightarrow \frac{U_H}{I} = B(\frac{-1}{ned}) \tag{4.4}$$

The charge carrier density can thus be calculated by measuring the Hall resistance, $R_H = U_H/I$, as a function of the magnetic field and determining the slope of this data.[30]

By assuming that the current is exclusively carried by electrons, the mobility of the charge carriers can be easily calculated if the carrier density is determined. Starting from the current density, the mobility can be calculated by:

$$j = en_s\mu \Rightarrow \mu = \frac{j}{en} = \frac{1}{en_s\rho} \Rightarrow \mu = \frac{I}{en_sV_x\frac{W}{L}} = \frac{L}{en_sR_lW} \tag{4.5}$$

For samples deposited at standard deposition settings (table 4.1) sheet carrier densities of $2 \cdot 10^{14}\ cm^{-2}$ are observed, which corresponds to 0.3 charge carriers per unit cell. For the mobility of the charge carriers values of the order of 1 $cm^{-2}V^{-1}s^{-1}$ are measured. A negative sign of the charge carriers was observed, from which it is concluded that the charge carriers are electrons.

Analysis of the sheet carrier density and mobility, provides additional information about the electronic properties of the interfaces. This makes it possible to find the origin of differences in resistivity. One can for example determine if a higher resistivity is caused by a decrease in sheet carrier density, or if the mobility of the charge carriers is limited.

Because of the large anisotropy of the resistance of $SrTiO_3/LaAlO_3$ interfaces grown on $LaSrAlTaO_3$ substrates, it is useful to perform Hall effect measurements at different angles. These measurements can provide information about the mobility of the charge carriers at different angles. Comparing the charge carrier density from different angles, also provides confirmation about the results. Assuming a homogenous interface, the charge carrier density should be constant and independent of the direction of measurement.

To perform hall effect measurements at different angles, the sample is structured with hall bar geometries at various angles. The layout of several of these geometries is shown in figure 4.11. In addition to the hall effect measurements, this layout can also be used to determine the anisotropy of the resistance by measuring the resistance of structures at various angles.

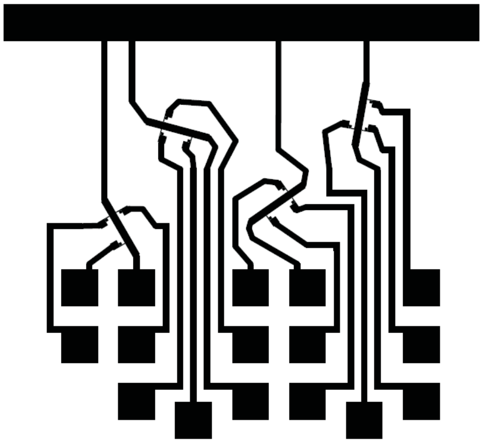

Figure 4.11 Hall bar measuring geometries at different angles for hall effect and anisotropy measurements

For several samples, Hall measurements were performed at different angles. An example of these measurements is shown in figure 4.12. The sheet carrier density and mobility are determined for two different angles. As expected, the sheet carrier densities determined for the two angles are comparable, while the difference in mobilities is more than one order of magnitude at low temperatures. So the difference in resistance is clearly caused by a difference in mobility of the charge carriers depending on the direction of the measurement geometry.

4.3.3 Measurement setups

Two different setups were used for the electrical characterization. For measurements that require an external magnetic field a PPMS setup was used. For anisotropy measurements and temperature dependent measurements, a flowcryostat with external equipment was used. These two different setups are shortly discussed in this section.

4.3.3.1 PPMS

For temperature and magnetic field dependent measurements, a physical property measurement system (PPMS) from Quantum Design was used. This is a commercially available system which

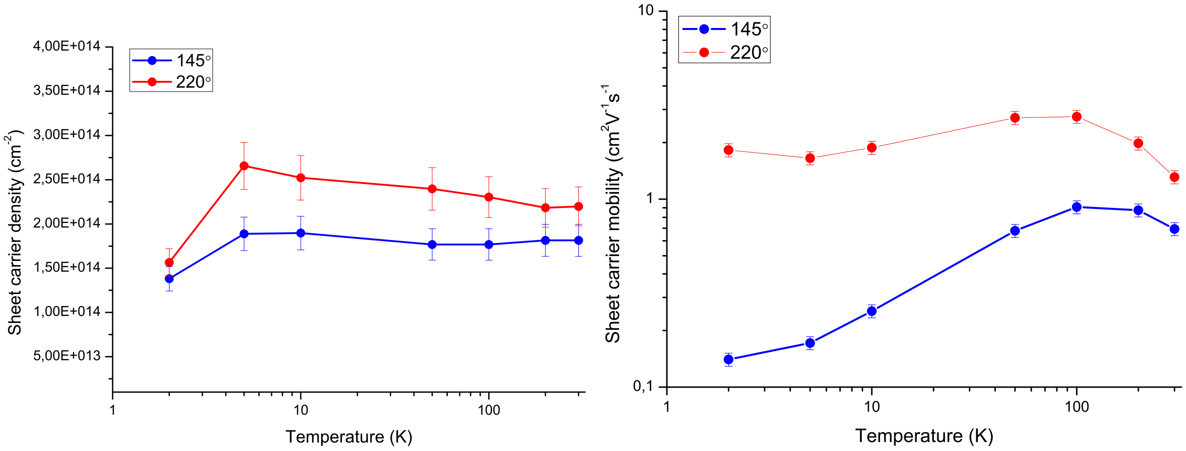

Figure 4.12 Hall effect measurements at two different angles. The sheet carrier density (left) and sheet carrier mobility (right) are shown. Sample was deposited at standard deposition settings (table 4.1) and a deposition pressure of 10^{-5} $mbar$ for the $LaAlO_3$ layer. 10 ML of $SrTiO_3$ and 10 ML of $LaAlO_3$ were deposited.

can be used for a variety of measurements. The sample holder connects to 12 electrical leads, and the system provides the possibility to measure up to 4 channels in one measurement run. The temperature at the sample can be controlled between 1.9 K and 400 K, with an accuracy of 0.2 % below 10 K and an accuracy of 0.02 % above 10 K. Magnetic field sweeps can be performed between -9 T and 9 T.

4.3.3.2 Flowcryostat

Because of the limited number of available electrical leads in the PPMS system, for the anisotropy measurements a different setup was used. A flow cryostat with an Oxford ITC4 temperature controller was used to control and measure the temperature. The insert for the cryostat provides 37 electrical leads, which gives the possibility to measure multiple channels in one measurement run. For the resistance measurements, a Keithley 2400 sourcemeter and a Keithley 2000 multimeter were used. In addition to the resistance measurements, IV-curves are measured for several samples. For the IV-curves a Keithley 2400 sourcemeter was used, which was controlled by a labview program.

Chapter 5

Results and discussion

As described in chapter 4, conducting $SrTiO_3/LaAlO_3$ interfaces were grown on $LaSrAlTaO_3$ substrates. Multiple samples were grown and structured for electrical analysis. These samples showed comparable resistance versus temperature dependence. In agreement with theory, large anisotropies were measured, with differences in resistance of more than one order of magnitude. Additionally, Hall effect measurements were performed at different angles. The sheet carrier densities determined from different angles were comparable and approximately $2.2 \cdot 10^{14}\ cm^{-2}$. The anisotropy is thus caused by different mobilities of the charge carriers depending on the direction. Relatively low mobilities of the order of $1\ cm^2V^{-1}s^{-1}$ were measured.

After establishing the possibility to grow interfaces with reproducible properties, several key parameters were studied. First of all the origin of the anisotropy was determined. Secondly, the influence of the width of the step edges was examined by using substrates with different miscut angles. Additionally, the deposition pressure of the $LaAlO_3$ layer and the thickness of the $SrTiO_3$ layer were studied. At last, the influence of the $SrTiO_3$ quality was investigated.

5.1 Origin of anisotropy

For several samples a comparable anisotropy as shown in figure 4.9(b) was measured. For these samples, the direction of minimum and maximum resistance corresponds to a direction parallel to the sample edges and show a periodicity of 90°. This leaves two obvious sources for the anisotropy, the crystal axes and the step and terrace structure (direction of the miscut angle). For standard $LaSrAlTaO_3$ substrates, the crystal axes and miscut direction coincide and are parallel to one of the substrate edges. Because $LaSrAlTaO_3$, $SrTiO_3$ and $LaAlO_3$ have a cubic crystal structure, no anisotropy with a 90° periodicity stemming from the crystal structure is expected. Assuming that the interface is truly two-dimensional, the step and terrace structure of the substrate plays a major role for the mobility of the charge carriers and is presumably the origin of the anisotropy.

In order to discriminate between the crystal axes and the miscut direction, a special batch of substrates with a different miscut direction was used. The miscut direction of these substrates was determined by atomic force microscopy and X-ray diffraction, and was rotated by 45° with respect to one of the edges of the sample. The direction of the crystal axes was determined by X-ray diffraction and was still parallel with the edges of the sample. This is schematically shown in figure 5.1 where the orientation of crystal structure and step and terrace structure are shown.

In this same figure the measured anisotropy at a temperature of 100 K is also shown. The minimum and maximum resistances are measured with geometries respectively parallel and perpendicular to the step edges. This suggests that the anisotropy is caused by the step and terrace structure at the interface. After all, the direction of the miscut and the anisotropy are now independent of the crystal structure.

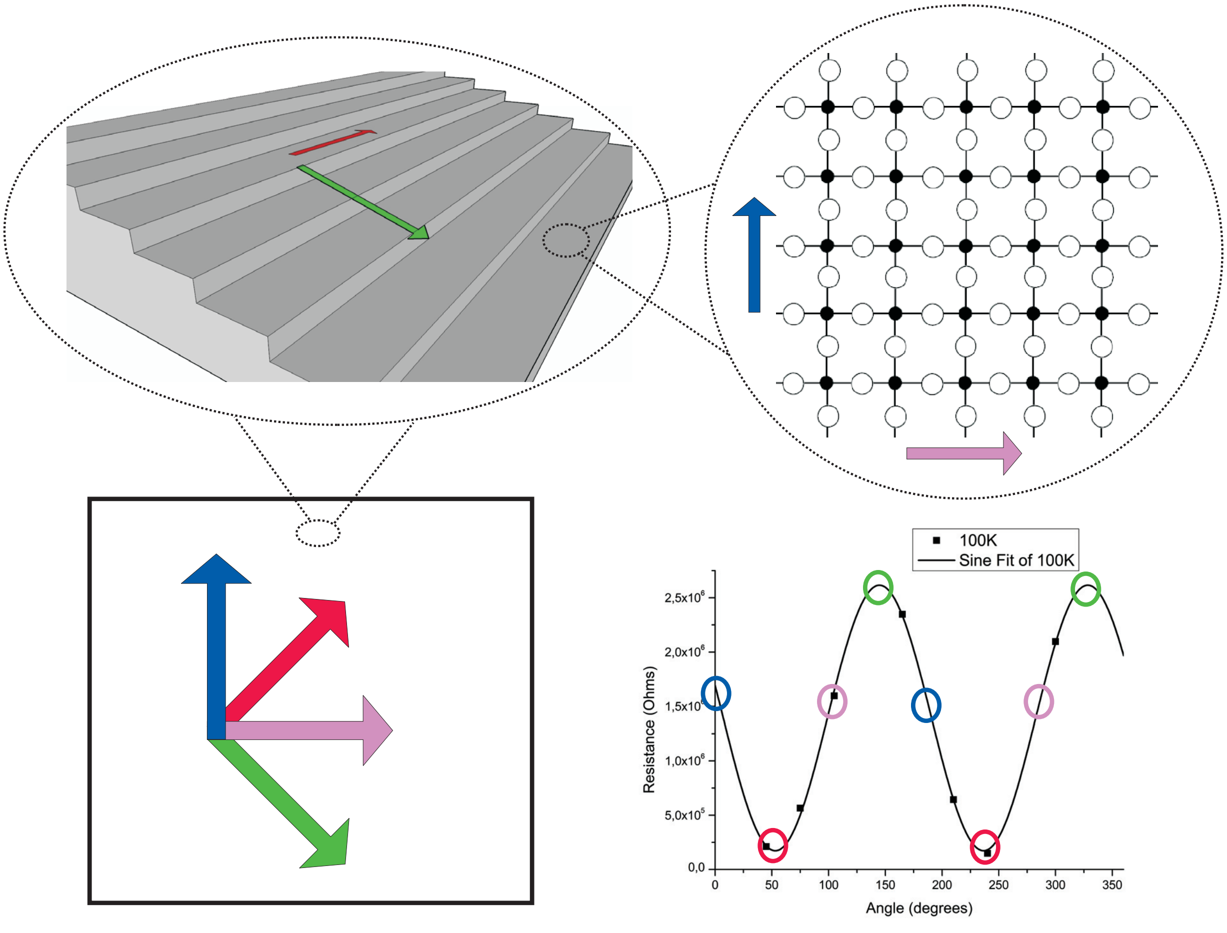

Figure 5.1 Layout of the sample (left bottom) with multiple directions indicated by the arrows. Part of the sample is enlarged (top left) to show the direction of the step and terrace structure (red and green arrows). Zooming in on part of one of the terraces (right top) reveals the crystal orientation (blue and pink arrows). The result of the anisotropy measurements is also shown (right bottom) and the four characteristic directions are indicated with colored circles. The maximum and minimum resistances correspond to the step and terrace structure.

Studying the anisotropy in more detail, one notices that the offset (the mean value) and the amplitude are of the same order. In fact, the relative anisotropy ($\frac{Amplitude}{Offset}$), which is 0.88 for this particular example, is between 0.5 and 1 for all samples. This is a strong indication that the conducting area is a (nearly) two-dimensional sheet. After all, the step edges are only located at the interface between $SrTiO_3$ and $LaAlO_3$. Based on atomic force microscopy measurements of the final $LaAlO_3$ interface, the interface consists of only or or two atomic layers. If all $SrTiO_3$ or $LaAlO_3$ layers would contribute to the overall conduction, the relative anisotropy would have been much weaker. If for example a total of 10 layers would contribute to the conduction, a relative anisotropy of the order of 0.1 would be expected. Because oxygen reduced $SrTiO_3$ becomes conducting, it is still possible that a small part of the $SrTiO_3$ layer is contributing to the overall conduction.

5.2 Miscut angle

In addition to the direction of the miscut angle, also the magnitude of the miscut angle is expected to determine the anisotropy. Intuitively one could argue that the charge carriers are scattered at the step edges. This would lead to the observed decrease in mobility perpendicular to the step edges. If this simple model holds, larger miscut angles (and smaller terraces) will increase the anisotropy. Three substrates with different miscut angles were chosen and 10 ML of $SrTiO_3$ and 10 ML $LaAlO_3$ were deposited with the same deposition parameters, as described previously (table 4.1).

After structuring the samples, anisotropy curves were measured. The anisotropies and corresponding sine fits at a temperature of 50 K are shown in figure 5.2(a). A difference in anisotropy is observed, however the largest anisotropy appears to be measured for the sample with the smallest miscut angle. Because there is also a large difference in offset (mean value) for these three samples, the fit results were studied in more detail. The relative anisotropy ($\frac{amplitude}{offset}$) was calculated, as shown in table 5.1. The relative anisotropy (also shown in figure 5.2(b))is comparable for a miscut angle of $0.05\,°$ and $0.20\,°$ and is significantly smaller for a miscut of $0.34\,°$. Still, the sample with the largest miscut angle shows the weakest anisotropy. This cannot be explained by a simple model where the charge carriers (confined to a two-dimensional sheet) are scattered at the step edges.

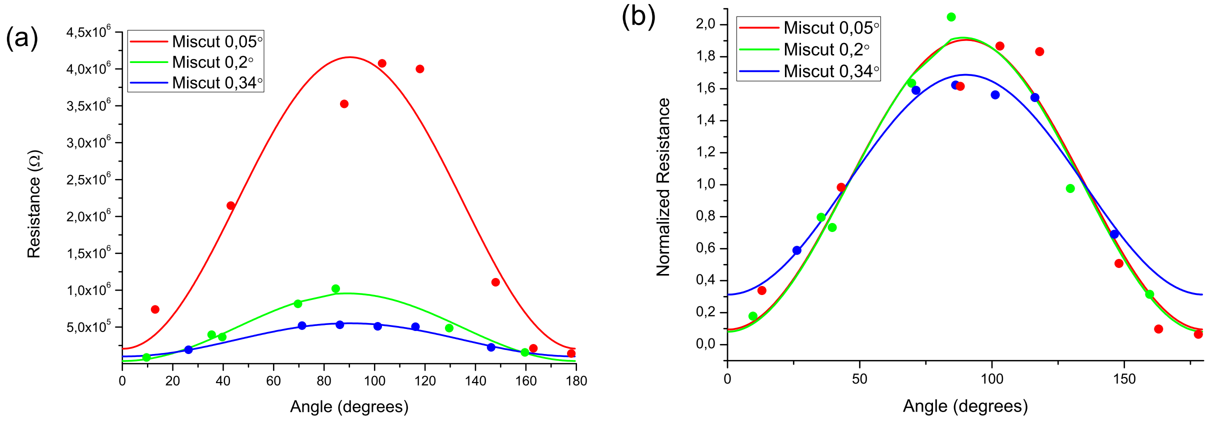

Figure 5.2 Measured (a) and normalized relative anisotropy (b) for different miscut angles of the substrate. The data is fitted with a sine function of $90\,°$.

Because no clear trend was observed for the samples with a different miscut angle, three additional samples were grown. These samples were structured with several Hall bar geometries at different angles to determine the sheet carrier density. Comparable values were obtained for all three samples as shown in figure 5.3(b). Any differences in resistance are therefore caused by different mobilities of the charge carriers.

Again the anisotropy was measured as shown in figure 5.3(a). A large difference in offset for the three samples is observed. To correct for this, the relative anisotropy is plotted (see

Table 5.1 Fit results for different miscut angles

	0.05 °	0.20 °	0.34 °
Amplitude	$2.0 \cdot 10^{6}$	$4.6 \cdot 10^{5}$	$2.2 \cdot 10^{5}$
Offset	$2.2 \cdot 10^{6}$	$5.0 \cdot 10^{5}$	$3.2 \cdot 10^{5}$
$\frac{Amplitude}{Offset}$	0.91	0.92	0.69

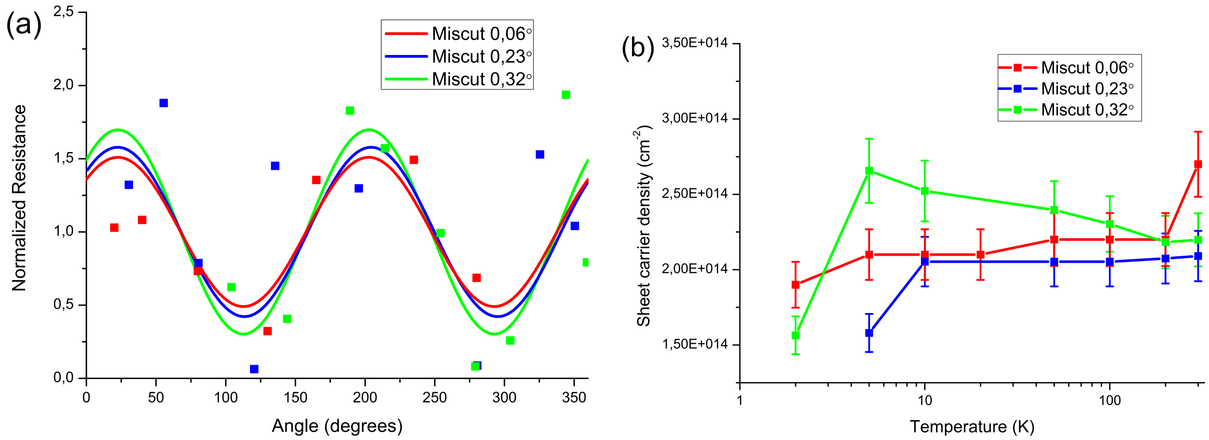

Figure 5.3 Relative anisotropy (a) and sheet carrier density (b) at a temperature of 50 K for different miscut angles. Samples were structured with several Hall bar geometries at different angles

also table 5.2). Now the expected behavior is observed. As the miscut angle increases, the relative anisotropy also increases. Note that the values of the resistance and relative anisotropy cannot be compared directly with the previous results, due to the difference in dimensions of the measurement geometries.

Table 5.2 Fit results for different miscut angles

	0.06 °	0.23 °	0.32 °
Amplitude	$5.7 \cdot 10^{4}$	$3.5 \cdot 10^{5}$	$5.2 \cdot 10^{4}$
Offset	$1.1 \cdot 10^{5}$	$6.1 \cdot 10^{5}$	$7.4 \cdot 10^{4}$
$\frac{Amplitude}{Offset}$	0.51	0.58	0.70
R_{step} [Ω]	130	210	23

Although the expected anisotropy behavior is observed for the last three samples, the error margin for the fits in figure 5.3(a) is relatively large. Especially for the sample with a miscut of $0,23\,^{\circ}$. If the simple model that charge carriers are scattered at the step edges is correct, crossing each individual step edge induces an additional resistance. In this case the resistance of a single step edge can simply be determined by the sine fit of each anisotropy curve. This results in the following fit function

$$R_s(\alpha) = R_0 + \frac{L_0 sin(\alpha) tan(\beta)}{c_{STO}} R_{step} \tag{5.1}$$

with L_0 the length of the measuring geometries (160 μm), α the angle between the geometry direction and terrace step direction, β the miscut angle of the substrate, and c_{STO} the lattice parameter of the SrTiO$_3$ unit cell ($3,905\ \mathring{A}$). The resulting R_0 and R_{step} provide the background resistance (or offset) and individual step resistance. The resulting values are given in table 5.2. Because both R_0 and R_{step} vary with approximately one order of magnitude, the simple model is not supported by these results. One possible explanation is a large sample to sample variation, however the sheet carrier densities for these samples is remarkably similar.

Another crucial parameter for the interface properties is the microscopic surface composition and roughness of the substrate before deposition. For some substrates, indications of half-unit cell steps around the step edges were found with atomic force microscopy. If there are indeed regions with a different surface termination, this will lead to a different type of interface, which is presumably insulating. Formation of insulating areas around the step edges could also lead to the observed anisotropy. However, these indications of a different surface termination was only observed for a few substrates and no systematic connection with the electrical properties was found.

5.3 LaAlO$_3$ deposition pressure

As already described in section 2.3.2 the deposition pressure of the LaAlO$_3$ layer is an important parameter for the electronic properties of SrTiO$_3$/LaAlO$_3$ interfaces on SrTiO$_3$ substrates. The same effect was investigated for these heterostructures grown on LaSrAlTaO$_3$ substrates. The deposition pressure of the SrTiO$_3$ layer was kept constant, while the LaAlO$_3$ layer was deposited at various pressures. By keeping the oxygen pressure during SrTiO$_3$ deposition constant at $1 \cdot 10^{-1}\ mbar$, the SrTiO$_3$ layer is assumed to be fully oxidized before depositing the LaAlO$_3$ layer. The deposition pressure of the LaAlO$_3$ layer was varied between $10^{-6}\ mbar$ and $10^{-4}\ mbar$.

No difference in structural properties was observed for the samples grown at different oxygen pressures. Layer thicknesses were controlled by RHEED and confirmed by X-ray diffraction. Atomic force microscopy showed comparable surfaces for all three samples.

The electronic properties showed some differences. The temperature dependence of resistance curves are shown in figure 5.4(a). For three deposition pressures, the R(T) curves of the minimum and maximum resistances are shown. It is clear that lowering the deposition pressure decreases the resistance, which is comparable to the heterostructures on SrTiO$_3$ substrates. The carrier density and mobility as a function of temperature for these samples are shown in figure 5.5, where for comparison the data of a 10 ML LaAlO$_3$ film on an SrTiO$_3$ substrate is also included.

Additionally, the anisotropy of the resistance was measured. For the sample grown at $10^{-4}\ mbar$ no good fit of the anisotropy could be obtained. However, some differences in resistance could be measured and the positions of the peaks roughly corresponded to the step and terrace structure. For the other two samples the anisotropy was determined at several temperatures. For a temperature of 50 K the relative anisotropy is shown in figure 5.4(b). The result of the fitting parameters is given in table 5.3. Both amplitude and offset are larger for the sample deposited at $10^{-5}\ mbar$. However, the relative amplitude ($\frac{amplitude}{offset}$) is larger for the sample deposited at $10^{-6}\ mbar$.

As mentioned in section 2.3.2, deposition at very low oxygen pressures ($10^{-6}\ mbar$) can lead to oxygen vacancies in the top layer of the SrTiO$_3$, due to irradiation damage from the incoming species. For SrTiO$_3$/LaAlO$_3$ interfaces grown on SrTiO$_3$ substrates, this leads to unusual high carrier densities and mobilities which was already pointed out by Ohtomo and Wang.[4] These high densities can only be explained by realizing that the layer of oxygen reduced SrTiO$_3$ also becomes conducting. Comparing this with the results obtained on LaSrAlTaO$_3$ substrates, a

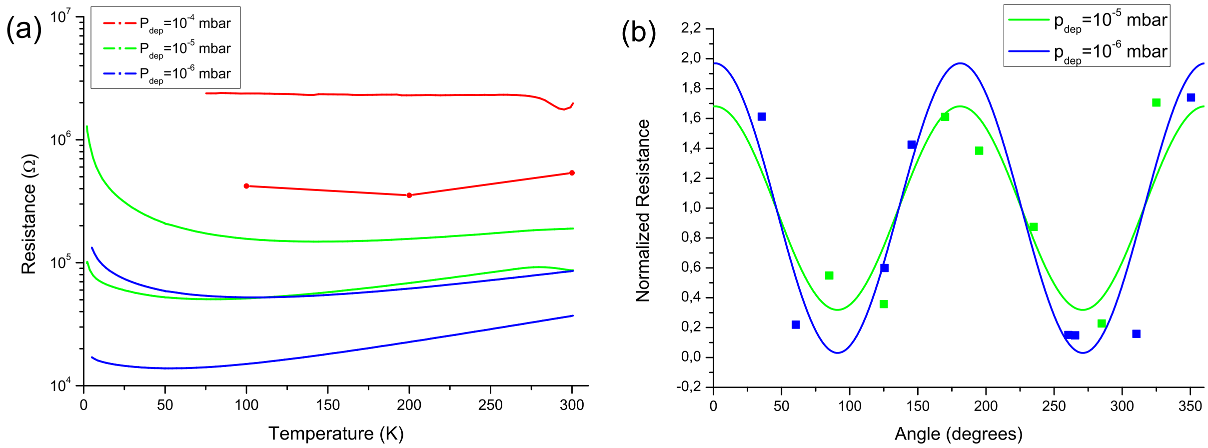

Figure 5.4 Minimum and maximum resistance as a function of temperature (a) and relative anisotropy at 50 K (b) for varying deposition pressure of the $LaAlO_3$ layer.

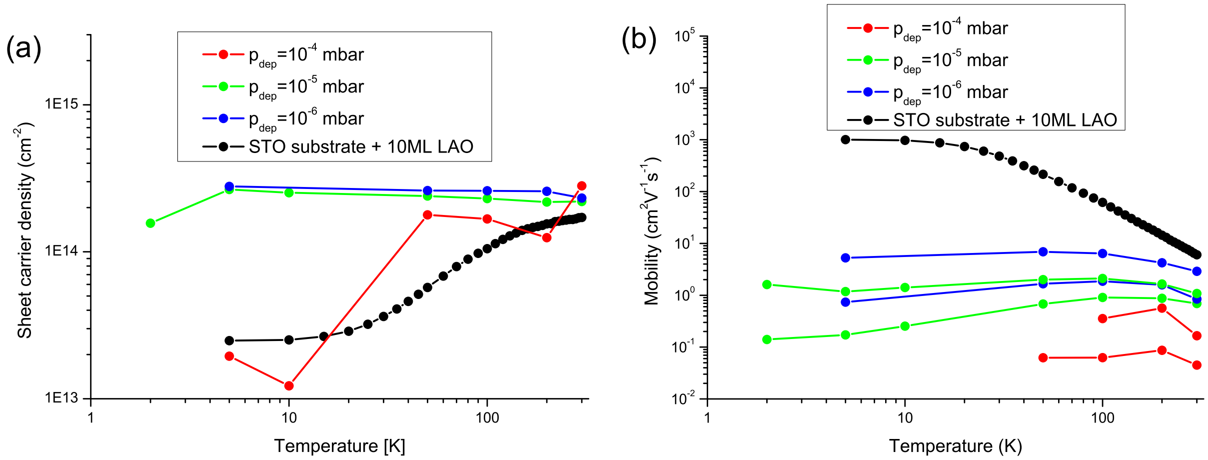

Figure 5.5 Sheet carrier density (a) and mobility (b) for different deposition pressures of the $LaAlO_3$ layer. For comparison, data from a 10 ML $LaAlO_3$ film on a $SrTiO_3$ substrate is added.

significant difference is observed. No difference in sheet carrier density was measured for samples deposited at 10^{-5} $mbar$ and 10^{-6} $mbar$ on $LaSrAlTaO_3$ substrates. This suggests that the conducting layer for samples deposited at 10^{-6} $mbar$ is still (nearly) two-dimensional and that no thicker layer of oxygen reduced $SrTiO_3$ was formed.

If a top layer of oxygen reduced $SrTiO_3$ would be formed, the thickness of this layer would presumably increase as the deposition pressure is lowered. An increasing thickness of the conducting layer would then lead to a decrease of the anisotropy. However, a stronger anisotropy is measured for the sample grown at the lowest deposition pressure, which indicates that there was no increase of the thickness of the conducting region. The anisotropy measurements therefore support the observation that no oxygen reduced layer is formed during $LaAlO_3$ deposition, even at low oxygen pressures of 10^{-6} $mbar$.

The sample deposited at a pressure of 10^{-4} $mbar$ shows a lower carrier density for temperatures below 50 K, suggesting carrier freeze out. The measured behavior is comparable with

Table 5.3 Fit results for different deposition pressures of the LaAlO$_3$ layer. Curves were fitted with a sine function with a period of 90 °.

	$P_{dep} = 10^{-5}\ mbar$	$P_{dep} = 10^{-6}\ mbar$
Amplitude	$5.7 \cdot 10^4$	$3.8 \cdot 10^4$
Offset	$8.4 \cdot 10^4$	$4.0 \cdot 10^4$
$\frac{Amplitude}{Offset}$	0.68	0.97

samples grown on SrTiO$_3$ substrates, as indicated in figure 5.5(a). In these samples carrier freeze effects are measured.

Because comparable sheet carrier densities are measured (for temperatures of 50 K and higher), differences in resistance are caused by a change in mobility of the charge carriers. Deposition at lower oxygen pressures, which presumably leads to more oxygen vacancies at the interface, leads to an increase of the mobility.

5.4 SrTiO$_3$ thickness and quality

To investigate the role of the SrTiO$_3$ layer, samples with different thicknesses were fabricated. A series with a SrTiO$_3$ layer thickness of 5 ML, 10 ML and 20 ML was fabricated. The layer thickness was in-situ monitored with RHEED and confirmed by X-ray diffraction. A comparable surface topograhpy was found in the atomic force microscopy images after growth.

Additionally, one sample with a different SrTiO$_3$ layer was used. For this sample, the SrTiO$_3$ layer was deposited by Hybrid Molecular Beam Epitaxy (hybrid MBE).[31] A similar treated substrate was used and atomic force microscopy images were taken before and after deposition. No difference is observed between the heated substrate and the deposited SrTiO$_3$ layer. A layer thickness of 22 ML was determined with X-ray diffraction for this sample. To compare this sample, a LaAlO$_3$ layer with a thickness of 10 ML was deposited at standard deposition parameters (see table 4.1).

These samples were structured with Hall bar geometries at various angles and the electronic properties were determined. Resistance versus temperature curves are shown in figure 5.6(a). In this figure the minimum and maximum resistances are plotted. Large differences are observed for the resistance, depending on the thickness or quality of the SrTiO$_3$ layer.

The anisotropy was measured and compared at several temperatures for these samples. The resulting relative anisotropies at a temperature of 50 K are shown in figure 5.6(b). Again, because of the large difference in offset of the resistance, the relative amplitude ($\frac{amplitude}{offset}$) was calculated and is given in table 5.4. The relative amplitude of the anisotropy is largest for the hybrid MBE sample. For the other three samples. For the PLD samples an increasing mean value (offset) is observed for increasing SrTiO$_3$ layer thicknesses.

Additionally, Hall measurements were performed to determine the sheet carrier density and carrier mobility for these samples. The resulting curves are shown in figure 5.7. The sheet carrier density is comparable for the samples with a SrTiO$_3$ thickness of more than 5 ML, and is nearly constant between 2 and 300 K. For the sample with a thickness of 5 ML, a lower sheet carrier density is observed below 50 K. The highest carrier mobility is observed for the hybrid MBE sample, which shows a maximum of 5 $cm^2V^{-1}s^{-1}$. The lowest mobilities are observed for the 5 ML and 10 ML thick STO layer.

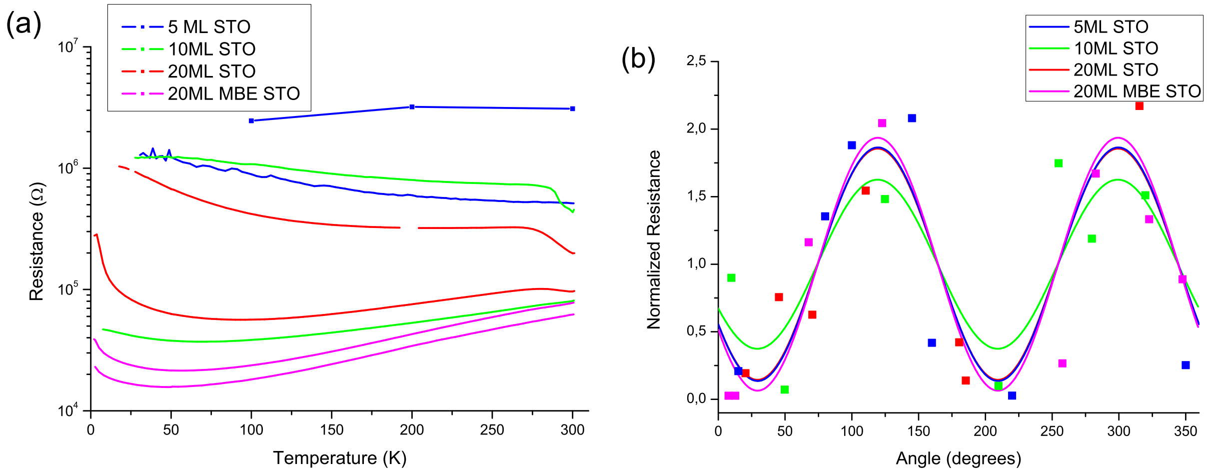

Figure 5.6 R(T) curves for the minimum and maximum resistances (a) and relative anisotropy at 50 K (b) for variation of the $SrTiO_3$ layer.

Table 5.4 Fit results for different deposition pressures of the $LaAlO_3$ layer. Curves were fitted with a sine function with a period of 90 °.

	5 ML STO	10 ML STO	20 ML STO	20 ML MBE STO
Amplitude	$1.6 \cdot 10^6$	$3.4 \cdot 10^5$	$3.9 \cdot 10^5$	$2.1 \cdot 10^4$
Offset	$1.8 \cdot 10^6$	$5.4 \cdot 10^5$	$4.6 \cdot 10^5$	$2.3 \cdot 10^4$
$\frac{Amplitude}{Offset}$	0.86	0.63	0.85	0.94

Overall, a thickness of only 5 ML of $SrTiO_3$ leads to a different behavior. The sheet carrier density is not constant over the measured temperature range, but decreases for temperatures lower than 50 K. For the other samples, the sheet carrier density shows comparable behavior. The differences in resistance are caused by a difference in carrier mobility, rather than density.

For the samples with a $SrTiO_3$ layer grown by pulsed laser deposition, no explanation was found for the difference in mobility, depending on $SrTiO_3$ layer thickness. For the samples from this series, the same substrate was used. A large 10×10 mm substrate was cut into 4 smaller pieces of 5×5 mm. These four pieces had the same substrate treatment, giving four similar substrates. Additionally, the same deposition parameters were used.

For the sample with the hybrid MBE $SrTiO_3$ layer, the highest carrier mobility is observed. Atomic force microscopy revealed an atomically flat surface of the $SrTiO_3$ layer. Apart from a slightly increased carrier mobility, the electronic properties show a comparable behavior with samples with pulsed laser deposited $SrTiO_3$ layers.

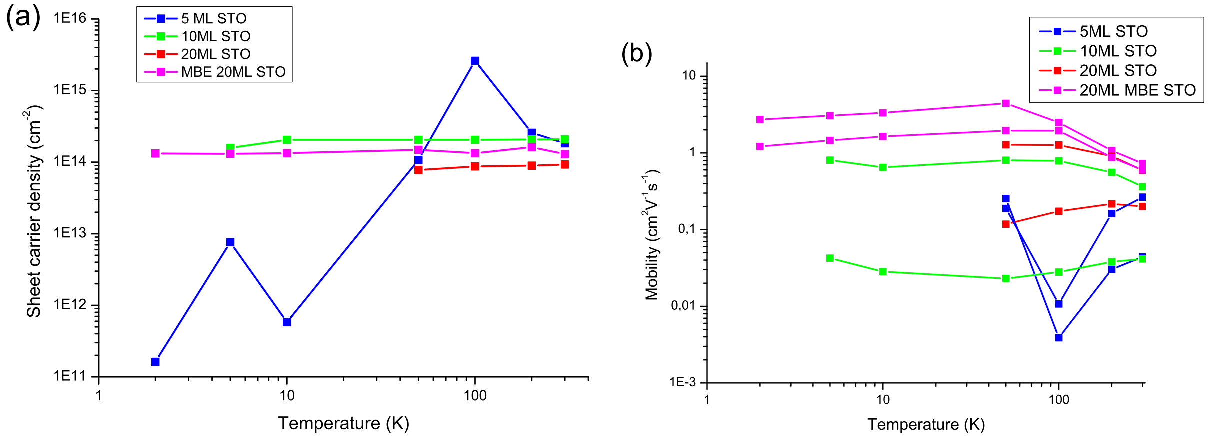

Figure 5.7 Sheet carrier density (a) and mobility (b) for variations of the SrTiO$_3$ layer

Chapter 6

Conclusions and Recommendations

6.1 Conclusions

$LaSrAlTaO_3$ was chosen as substrate for the growth of conducting $SrTiO_3/LaAlO_3$ interfaces because of its suitable lattice parameter and cubic structure. A suitable substrate treatment was developed which results in a well defined step and terrace structure at the surface, with unit cell step heights indicating a single terminated surface.

$SrTiO_3$ and $LaAlO_3$ layers were successfully deposited on treated $LaSrAlTaO_3$ substrates. Comparing the surface topography before and after deposition a minimum increase of surface roughness was observed and the step and terrace structure is still clearly visible. The layer thickness, which was in-situ monitored by RHEED, was confirmed by X-ray diffraction.

The goal to grow conducting $SrTiO_3/LaAlO_3$ interfaces on a different substrate was fulfilled. Although the measured resistances are higher compared to the interfaces on $SrTiO_3$ substrates, a comparable or even higher sheet carrier density at room temperature was observed for interfaces grown on $LaSrAlTaO_3$ substrates. For the interfaces grown on $SrTiO_3$ substrates, the sheet carrier density shows a strong decrease for lower temperatures, while it is nearly constant for the interfaces grown on $LaSrAlTaO_3$ substrates. The large difference in resistance is caused by a difference of the mobility of the charge carriers. For the interfaces grown on $SrTiO_3$ substrates, mobilities of the order of $10^3\ \frac{cm^2}{Vs}$ are observed, while for the interfaces on $LaSrAlTaO_3$ substrates the observed mobilities are of the order of $1\ \frac{cm^2}{Vs}$. This difference could be caused by differences in $SrTiO_3$ quality for substrates and grown layers. Although the substrates and grown layers are structurally comparable, a larger number of defects can be expected in the grown layer, leading to different properties such as the dielectric constant. For $SrTiO_3$ substrates the dielectric constant increases from approximately 300 at room temperature up to 20000 at low temperatures. For $SrTiO_3$ films grown with pulsed laser deposition the dielectric constant remains nearly constant at 300 for the same temperature range.

The expected directional anisotropy of the resistance is observed for the interfaces grown on $LaSrAlTaO_3$ substrates. By using substrates with a different miscut direction, the step and terrace structure at the interface was determined as the origin of the anisotropy. This additionally suggests that the conducting region is confined to a (nearly) two-dimensional sheet at the interface, because of the strength of the anisotropy.

By depositing the $LaAlO_3$ layer at various pressures, the role of oxygen vacancies was studied. At the lowest deposition pressure of $10^{-6}\ mbar$, the sheet carrier density remained below the theoretical maximum of 0,5 electron per unit cell and showed comparable values with samples deposited at 10^{-5} *mbar*. Additionally, a strong anisotropy was measured for this sample, comparable to samples grown at different oxygen pressures. These two observations both suggest that the conducting region is still two-dimensional. Still, a difference in resistance was observed depending on deposition pressure. An increase in deposition pressure leads to an increase of the resistance caused by a change in mobility of the charge carriers. For a deposition pressure of 10^{-4} *mbar* carrier freeze out was observed, while for lower deposition pressures the sheet carrier density remains constant over the measured temperature range.

Growing conducting $SrTiO_3/LaAlO_3$ interfaces on a different substrate material also provides the unique possibility to investigate the influence of the $SrTiO_3$ layer. The influence of the thickness and quality of the $SrTiO_3$ layer was investigated. Samples with a thickness of 5 ML, 10 ML and 20 ML were fabricated. Additionally, for one sample a 20 ML thick hybrid MBE $SrTiO_3$ layer was used. For a $SrTiO_3$ thickness of 5 ML the sheet carrier density showed a decrease for temperatures below 100 K, for all other samples a nearly constant sheet carrier density was observed over the temperature range of $2 - 300$ K. An increase in resistance was observed for thinner $SrTiO_3$ layers. The lowest resistances are measured for the hybrid MBE $SrTiO_3$ sample. These differences in resistance are predominantly caused by differences in carrier mobilities.

6.2 Recommendations

In addition to the study of the conducting interfaces on $LaSrAlTaO_3$ substrates, it would be interesting to fabricate the opposite type of interface termination. To grow this interface, a substrate with the different surface termination is required, or an intermediate layer would be deposited which induces a termination switch. $SrRuO_3$ is shown to be a suitable material to induce this termination switch, due to the volatility of the Ruthenium.[32] This test can be used to confirm that the conduction is confined at the interface.

To study the influence of strain, one should include a series of samples where comparable $SrTiO_3$ and $LaAlO_3$ layer are deposited on $SrTiO_3$ substrates. At these $SrTiO_3$ substrates, strain effects in the $SrTiO_3$ layer are eliminated and an absolute single surface termination for the substrates can be achieved.

Although magnetoresistance effects were not studied in detail, some interesting results were obtained. For several samples a change of sign for the magnetoresistance was observed around 100 K. Additionally, depending on the direction of measurements, a difference in behavior was observed at low temperatures. For a direction parallel with the step edges a constantly decreasing resistance was measured for increasing magnetic fields. However, for different directions a local minimum was observed around a magnetic field of 2 T. An example of this is shown in figure 6.1. This remarkable difference is thought to originate from different carrier mobilities, but it is worthwhile to further investigate these features.

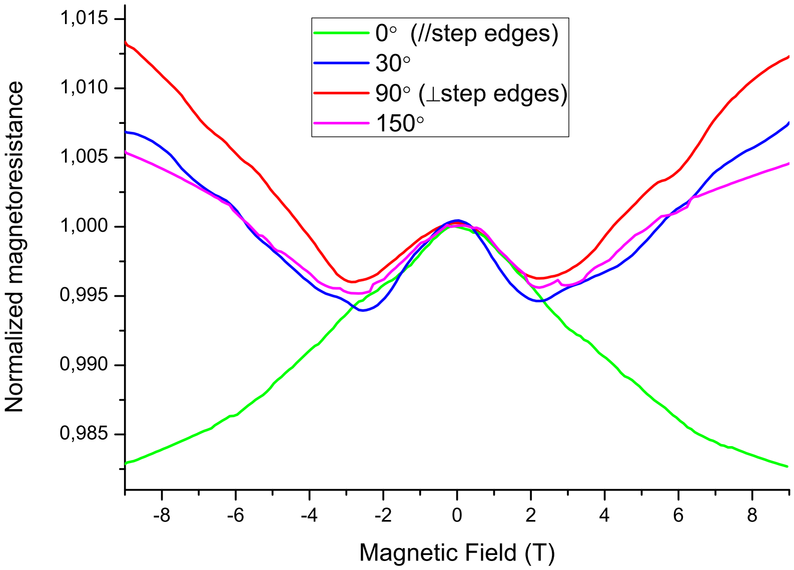

Figure 6.1 Magnetoresistance at a temperature of 2 K for different directions for 10 ML $SrTiO_3$ and 10 ML $LaAlO_3$ deposited at standard deposition parameters (table 4.1).

Bibliography

[1] J. Bednorz and K. Müller, “Possible high tc superconductivity in the ba-la-cu-o system,” *Z. Phys. B*, vol. 64, no. 1, pp. 189–193, 1986.

[2] R. Cava, R. van Dover, B. Batlogg, and E. Rietman, “Theory of high-tc superconductivity in oxides,” *Phys. Rev. Lett.*, vol. 58, pp. 2794–2797, May 1987.

[3] M. Wu, J. Ashburn, C. Torng, P. Hor, R. Meng, L. Gao, Z. Huang, Y. Wang, and C. Chu, “Superconductivity at 93 k in a new mixed-phase y-ba-cu-o compound system at ambient pressure,” *Phys. Rev. Lett.*, vol. 58, pp. 908–911, March 1987.

[4] A. Ohtomo and H. Wang, “A high-mobility electron gas at the $LaAlO_3$/$SrTiO_3$ heterointerface,” *Nature*, vol. 427, pp. 423–426, January 2004.

[5] G. Hassink, *Two-dimensional electron layers in perovskite oxides.* PhD thesis, University of Twente, the Netherlands, 2009.

[6] M. Huijben, A. Brinkman, G. Koster, G. Rijnders, H. Hilgenkamp, and D. H. Blank, “Structure-property relation of $SrTiO_3$/$LaAlO_3$ interfaces,” *Adv. Mat.*, vol. 21, 2009.

[7] A. Bhalla, G. Ruyan, and R. Rustum, “The perovksite structure - a review of its role in ceramic science and technology,” *Mat. Res. Innovat.*, vol. 4, pp. 3–26, July 2000.

[8] G. Koster, G. Rijnders, D. H. Blank, and H. Rogalla, “Surface morphology determined by (001) singe-crystal $SrTiO_3$ termination,” *Physica C*, vol. 339, pp. 215–230, May 2000.

[9] M. Huijben, *Interface Engineering for Oxide Electronics.* PhD thesis, University of Twente, the Netherlands, 2006.

[10] H. Lehnert, H. Boysen, J. Schneider, F. Frey, D. Hohlwein, P. Radaelli, and H. Ehrenberg, “A powder diffraction study of the phase transition in $LaAlO_3$,” *Z. Kristrallogr.*, vol. 215, p. 536, Sep 2000.

[11] S. Hayward, F. Morrison, S. Redfern, E. Salje, J. Scott, K. Knight, S. Tarantino, A. Glazer, V. Daniel, M. Zhang, and M. Carpenter, “Transformation processes in $LaAlO_3$: Neutron diffraction, dielectric, thermal, optical and raman studies,” *Phys. Rev. B*, vol. 72, 2005.

[12] N. Nakagawa, H. Y. Hwang, and D. A. Muller, “Why some interfaces cannot be sharp,” *Nature Materials*, vol. 5, pp. 204–209, Mar 2006.

[13] J. Nishimura, A. Ohtomo, O. A., Y. Murakami, and M. Kawasaki, “Controlled carrier generation at a polarity-discontinued perovskite heterointerface,” *Jpn. J. Appl. Phys.*, vol. 43, 2004.

[14] A. Kalabukov, R. Gunnarsson, J. Borjesson, E. Olsson, and D. Claeson, "Effect of oxygen vacancies in the $SrTiO_3$ substrate on the electrical properties of the $LaAlO_3/SrTiO_3$ interface," *Phys. Rev. B*, vol. 75, no. 12, 2007.

[15] A. Brinkman, M. Huijben, M. van Zalk, J. Huijben, U. Zeitler, J. Maan, W. van der Wiel, G. Rijnders, D. Blank, and H. H. *Nature Materials*, vol. 6, 2007.

[16] N. Reyren, A. Caviglia, L. Fitting Kourkoutis, G. Hammerl, C. Richter, C. Schneider, T. Kopp, A.-S. R/"uetschi, D. Jaccard, M. Gabay, D. Muller, J.-M. Triscone, and J. Mannhart, "Superconducting interfaces between insulating oxides," *Science*, vol. 317, pp. 1196–1199, Aug 2007.

[17] S. Thiel, G. Hammerl, A. Schmehl, C. Schneider, and J. Mannhart, "Tunable quasi two-dimensional electron gases in oxide heterostructures," *Science*, vol. 313, pp. 1942–1945, Sep 2006.

[18] "www.crystec.de."

[19] P. Padhan, P. LeClair, A. Gupta, and G. Srinivasan, "Magnetodielectric response in epitaxial thin films of multiferroic Bi_2NiMnO_6," *Journal of Physics: Condensed Matter*, vol. 20, Aug 2008.

[20] M. Okatan, C. Weiss, and S. Alpay, "Pyroelectric properties of epitaxial (001) barium strontium titanate as a function of space charge density," *Integrated Ferroelectrics*, vol. 111, pp. 80–87, 2009.

[21] R. Matyi, W. Doolittle, and A. Brown, "High resolution x-ray diffraction analyses of gan/$LiGaO_2$," *J. Phys. D: Appl. Phys.*, vol. 32, pp. A61–A64, 1999.

[22] K. Young and D. Strother, "Microwave performance of epitaxial YBCO films on $YAlO_3$ (001) substrates," *Physica C*, vol. 208, pp. 1–6, Jan 1993.

[23] V. Leca, *Heteroepitaxial growth of copper oxide superconductors by pulsed laser deposition.* PhD thesis, University of Twente, the Netherlands, 2003.

[24] B. Jalan, R. Engel-Herbert, N. J. Wrigth, and S. Stemmer, "Growth of high-quality $SrTiO_3$ films using a hybrid molecular beam epitaxy approach," *J. Vac. Sci. Technol. A*, vol. 27, pp. 461–464, May/Jun 2009.

[25] T. Ohnishi, K. Takahashi, M. Nakamura, M. Yoshimoto, and H. Koinuma, "A-site layer terminated perovskite substrate: $NdGaO_3$," *Applied Physics Letters*, vol. 74, pp. 2531–2533, Apr 1999.

[26] R. Eason, *Pulsed Laser Deposition of Thin Films.* Wiley, 2006.

[27] T. Okada, Y. Nakata, M. Maeda, and W. Kumuduni, "Ultraviolet laser light scattering diagnostics of the plume in pulsed-laser deposition process," *Journal of Applied Physics*, vol. 82, 1997.

[28] M. Ohring, *Materials Science of Thin Films: Deposition and Structure.* Academic Press, second ed., 2002.

[29] C. Pang, P. Hing, and A. See, "Application of phase-imaging tapping-mode atomic-force microscopy to investigate the grain growth and surface morphology of $TiSi_2$," *J. Vac. Sci. Techn. B*, vol. 20, pp. 1866–1869, Sep/Oct 2002.

[30] H. Ibach and H. Lüth, *Solid-State Physics, An Introduction to Principles of Materials Science.* Springer Verlag, 2003.

[31] In collaboration with Bharat Jalan and Susanne Stemmer, University of California, Santa Barbara; Ramesh Lab, University of California, Berkeley.

[32] G. Rijnders, D. H. Blank, J. Choi, and C.-B. Eom, "Enhanced surface diffusion through termination conversion during epitaxial srruo growth," *Appl. Phys. Let.*, vol. 84, pp. 505–507, Jan 2004.